Modeling Realistic Structures of Trimetallic Nanoalloy Catalysts Using Chemically Meaningful Descriptors

*Arravind Subramanian, Mikhail V. Polynski, Mathan K. Eswaran, Sergey M. Kozlov[1]**

[1] Department of Chemical and Biomolecular Engineering, National University of Singapore, 4 Engineering Drive 4, Singapore 117585, Singapore.

AUTHOR INFORMATION

Corresponding Author

* sergey.kozlov@nus.edu.sg

ORCID

Arravind Subramanian: 0009-0009-7381-3612

Mikhail V. Polynski: 0000-0002-5559-0066

Mathan K. Eswaran: 0009-0008-2754-6122

Sergey M. Kozlov: 0000-0002-7765-4649

ABSTRACT

The computational design of alloy catalysts is hindered by the uncertainty in their structure and arrangement of constituent elements within the lattice of catalyst particles, i.e., their chemical ordering. Moreover, chemical ordering in alloy nanoparticles (nanoalloys) can be affected by the reaction temperature due to thermal disorder. In this study, we develop a method for realistic simulations of trimetallic alloy nanocrystallites with the lowest energy chemical ordering or

chemical ordering taking into account thermal disorder in the nanoalloy. This method is based on Monte Carlo simulations using topological lattice Hamiltonian, whose parameters are fitted to the results of density functional (DFT) simulations of thoughtfully designed archetypal nanoalloy structures. The implementation of this method in Python code is freely available online. Using this method, we characterized chemical orderings in nanoparticles composed of 79 and 338 atoms of metals with known catalytic activity in CO_2 hydrogenation, namely, Pd-Pt-Cu, Ni-Pd-Cu, and Co-Rh-Cu. Our simulations show that the thermal disorder in these alloys significantly affects the composition of surface sites. Such structural changes are demonstrated to affect the average binding energies of reaction intermediates to the catalyst surface by up to 1.1 eV, implying their critical effect on the alloy's catalytic properties. Moreover, we demonstrate how the developed code can be used for brute-force evaluation of entropic contributions to mixing free energies in alloy nanoparticles. The demonstrated abilities of the proposed method to generate realistic models of trimetallic nanoalloys in a computationally efficient manner enable reliable simulations of catalytic properties of trimetallic catalysts for their in-depth understanding and computational design.

1. INTRODUCTION

The development of heterogeneous catalysts has evolved to include increasingly complex systems, such as single-atom,[1,2] dual atom,[3–6] bimetallic,[7,8] and trimetallic alloy nanoparticle (NP) catalysts.[9] In particular, trimetallic alloys often exhibit promising catalytic properties due to the abundance of polymetallic active sites, controllable effects of the alloying on the electronic structure and activity of the catalyst[10–12] as well as their ability to catalyze reactions through qualitatively new mechanisms.[13,14] For example, trimetallic catalysts could be employed[9] in many processes deemed crucial for global economic development and sustainability, including the

hydrogenation of CO and CO_2 into high-value alcohols and hydrocarbons,[15–18] key dehydrogenation processes such as those involving formic acid[19–21] and ammonia borane[22–24] for hydrogen storage, and selective oxidations such as the conversion of methane to methanol.[25] Moreover, trimetallic alloys can also be used as precursors for the production of metal@oxide core@shell nanoparticles for catalytic and other applications through controlled oxidation.[26,27]

The growing structural complexity of trimetallic alloy nanoparticles (nanoalloys) presents a significant challenge for computational catalyst design, simulations of catalytic reaction mechanisms, and electronic structure studies aimed at supporting experimental research. Indeed, reliable simulations require the identification of a realistic catalyst model among countless tentative structures[28] with widely varying catalytic properties. Several computational strategies were employed to address this challenge. Integrating forcefield-based molecular dynamics or metadynamics with subsequent DFT optimizations is a popular approach that can predict chemical ordering and nanoparticle shape.[29–31] For nanoparticles comprising up to several hundreds of atoms, global optimizations employing machine learning potentials and genetic algorithms are often preferred.[32,33] In principle, empirical force fields can be used to study structures of even bigger NPs,[28,34–36] yet the wide range of chemical environments within a nanoparticle and the diversity of atom-atom interactions complicate the selection of an accurate forcefield or require its re-parameterization for the given task.

Fortunately, for bigger nanoparticles the problem of computational structural characterization of alloy nanoparticles can be alleviated due to their crystalline structure, which is typically experimentally observed in NPs with a few nm in size.[37,38] In this case, the challenge of identifying the realistic alloy particle structure is transformed to optimizing the chemical ordering of elements within the predefined crystalline lattice, i.e., identifying the most thermodynamically stable

homotop.[39] However, identifying realistic chemical ordering in moderately sized nanoalloys still requires extremely computationally efficient techniques due to an extremely high number of tentative homotops, e.g., around 10^{35} for an $A_{26}B_{26}C_{27}$ nanocrystallite. Among these, only one structure has the lowest energy, which will be obtained by the catalyst at low temperatures in thermodynamic equilibrium. In bulk metals, the chemical ordering is typically simulated using lattice Hamiltonians constructed using the cluster expansion framework.[40–42] However, the application of such techniques to nanoparticles is rare.[43,44]

The bond-centric model has been recently proposed as a new approach that utilizes bond dissociation energies from metallic dimers for NP energy evaluations.[45] This model, combined with genetic algorithm optimizations, is suitable for optimizing chemical ordering in multimetallic NPs.[46,47] For example, the bond-centric model was effectively applied to predict the energies of various shapes of Rh nanoparticles, which are active in the CO methanation reaction step,[48] as well as to calculate binding energies of catalytic intermediates to pure and alloy nanoparticles.[49]

Among various techniques, the TOP method[37] stands out due to its extreme computational efficiency and straightforward physical interpretation of its parameters reflecting the "topology" of the nanoalloy, i.e., heteroatomic bond formation and surface segregation of alloy components. Most importantly, its applicability was demonstrated for a wide range of bimetallic alloys with various types of structures, including complete[50,51] or incomplete[52,53] core-shell, layered[37] and phase-separated alloys,[54] as well as different kinds of intermediate structures.[55] Briefly, this method screens various nanoalloys structures through the Metropolis Monte-Carlo algorithm by approximating the nanoalloy energy using a lattice Hamiltonian, whose parameters are fitted to the results of several dozen DFT calculations of nanoalloys with the same composition.

In this study, we extend the TOP method to the optimization of chemical ordering in trimetallic nanoalloys and apply it to the computational characterization of the structures of Ni-Pd-Cu, Pd-Pt-Cu, and Co-Rh-Cu trimetallic nanoparticles with very different types of chemical ordering. We explore the structures of these alloys because their constituent elements are known for high catalytic activity in a diverse range of reactions, including CO_2 hydrogenation.[56] Cu is chosen as the foundational element in all considered alloys due to its proven catalytic efficiency of Cu-containing catalysts in CO_2 hydrogenation to liquid fuels,[57] its relative abundance, and its capacity to form stable alloy nanoparticles with numerous metals.[9] In selecting other metals, we give preference to metals that can facilitate CO_2 hydrogenation by promoting elementary steps such as C≡O and -CHO insertion (Co and Rh, as well as Cu), [58,59] C≡O hydrogenation (the Cu-Pd pair),[13] and C-O bond cleavage (e.g., Co, Ni, Pd, as well as Cu).[60–63] All these metals have been utilized in mono- and multimetallic CO and CO_2 hydrogenation catalysts. [57,59] In particular, Co-Cu and Rh-Cu alloys were proposed for CO hydrogenation to higher alcohols and oxygenates, respectively, based on DFT calculations.[64,65]

The activity of Pd-Pt-Cu alloys has been studied in such reactions as electrochemical CO_2 reduction, oxygen reduction, and alcohol oxidation reactions.[66,67] In addition, Co-Rh-Cu alloys were active in the electrochemical NH_3BH_3 decomposition,[68] whereas Ni-Pd-Cu alloys have been studied as components of hydrogen separation membranes and catalysts for electrochemical oxygen reduction reaction.[69–71]

Similarly to the TOP method for bimetallic nanoparticles,[37] the extended method accounts for thermal disorder in the alloy models under reaction conditions and enables the design of reliable models of trimetallic catalysts for further detailed simulations. Moreover, this method requires a limited number of DFT calculations to achieve good precision and accuracy of simulations (i.e.,

below the energy of thermal disorder). We show that the thermal disorder significantly changes the surface structure of the considered alloy nanoparticles and the composition of active sites available on the alloy surface, affecting catalyst reactivity and stability under reaction conditions.

2. COMPUTATIONAL METHODOLOGY

2.1 The extension of the TOP method to trimetallic nanoparticles. In this study, we propose describing the relative energies of trimetallic A-B-C alloy nanocrystallites using the following extended TOP lattice Hamiltonian describing the "topology" of the nanoalloy:

$$E_{TOP} = E_0 + \varepsilon_{BOND}^{A-B} N_{BOND}^{A-B} + \varepsilon_{BOND}^{B-C} N_{BOND}^{B-C} + \varepsilon_{BOND}^{A-C} N_{BOND}^{A-C} + \sum_{n=6,7,9} \varepsilon_n^A N_n^A + \sum_{n=6,7,9} \varepsilon_n^B N_n^B \qquad (1),$$

In this formula, E_0 is a constant minimizing the difference between nanoalloy energies calculated using TOP Hamiltonian and DFT calculations. In turn, the second, third, and fourth terms in this formula reflect the contributions of N_{BOND}^{A-B}, N_{BOND}^{B-C} and N_{BOND}^{A-C} heteroatomic bonds formed between elements A and B, B and C, and A and C, respectively, to the nanoparticle energy. In turn, the last two sums reflect the contributions from N_n^A and N_n^B undercoordinated atoms of type A and B with coordination number n to the nanoalloy stability. For example, in a truncated octahedral nanoparticle with fcc structure, coordination numbers n of 6, 7, and 9 correspond to atoms on the corner, edge, and (1 1 1) facet, whereas bulk atoms have coordination number 12 (Figure 1). Other coordination numbers may be present in nanoparticles of other shapes or with other lattice types, which can also be simulated using the present method by adjusting the shape of the last two terms in equation (1) to a particular case under consideration. Each structural descriptor N_Y^X in this formula is multiplied by a corresponding energetic descriptor ε_Y^X, reflecting how each structural feature contributes to the stabilization ($\varepsilon_Y^X < 0$) or destabilization of the

nanoparticle ($\varepsilon_Y^X > 0$). Similar to the TOP method for bimetallic alloys,[37] the proposed lattice Hamiltonian contains neither contributions from homoatomic bonds A-A, B-B, and C-C nor contributions from undercoordinated atoms of type C. These terms are omitted because the respective structural descriptors N_{BOND}^{X-X} $(X = A, B, C)$ and N_n^C would not be linearly independent of the descriptors already present in the formula for the chosen size and shape of the nanoparticle lattice Hamiltonian, which would make the fitting procedure ambiguous. As a result, ε_{BOND}^{X-Y} parameters in equation (1) should be interpreted as the relative energy of heteroatomic X-Y bonds compared to monoatomic X-X and Y-Y bonds. In turn, the descriptors ε_n^X should be interpreted as the energy change due to the substitution of atom C on a site with coordination number n by atom X.

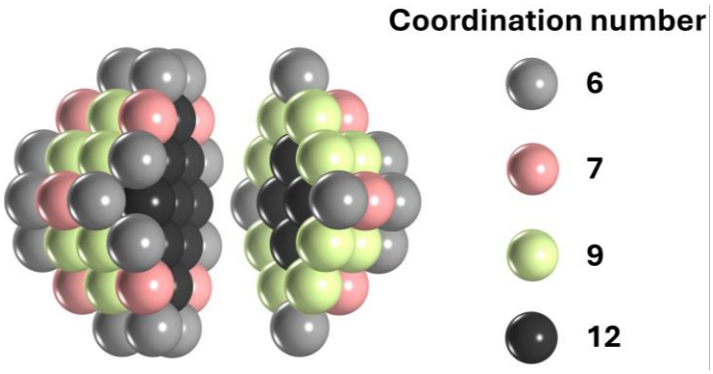

Figure 1. Various coordination numbers of atoms in 79-atom truncated octahedral nanoparticles with fcc structure.

2.2. Fitting of the TOP Hamiltonian to DFT results. For each nanoalloy composition, energetic descriptors in equation (1) can be fitted to approximate the energies of alloy nanoparticles from DFT calculations via linear regression procedure. To make the fitting more robust, we assembled a training set composed of 132 distinct homotops of trimetallic nanoparticle structures with archetypal chemical orderings that can be expected based on chemical intuition (Figure S1).

For example, these archetypal homotops include structures where the number of A-B, B-C, or A-C bonds is either high or low due to their strong exothermicity or endothermicity. We have also included structures where a specific element A, B, or C occupies as many (or as few) as possible corner sites, edge sites, or terrace sites in the nanoparticle due to its strong preference for (or against) segregation on low-coordinated sites. These archetypal structures were prepared by performing optimization of chemical ordering in A-B-C nanoalloys using simplified lattice Hamiltonian from equation (1), where most energetic descriptors ε_Y^X were assumed to be 0 and only one or two energetic parameters ε_Y^X had extremely high positive or negative values above 10 eV in magnitude (see Appendix in the Supplementary Information). All the archetypal structures can be generated using the code on the project's GitHub page.[72] Since most existing nanoalloys have numerous energetic descriptors ε_Y^X with moderate values (between 0 and 10 eV), their low-energy structures could be regarded as some intermediate configurations *interpolated* between the archetypal nanoalloy structures. In this way, we ensure that the performed optimization of chemical ordering in nanoalloys does not involve the *extrapolation* of the TOP Hamiltonian beyond its training set, which, in our experience, improves the robustness and the accuracy of the fitting.

It is essential to highlight that this set of 132 structures is independent of the identities of elements in a trimetallic nanoalloy but depends on their ratios in the nanoparticle composition as well as on the size and shape of the NP. That is, we performed DFT calculations on the same set of 132 archetypal trimetallic nanoalloy structures to generate a training set for fitting of the lattice Hamiltonian for each Ni-Pd-Cu, Pd-Pt-Cu, and Co-Rh-Cu alloy (396 calculations total). In the calculations, atoms A, B, and C in each archetypal structure were replaced with the actual elements of the alloy and then subjected to spin-polarized DFT geometry optimization using computational

parameters described later in this section. Thus, the employed lattice Hamiltonians are fitted to the results of DFT calculations, taking into account the contribution of structural deformation and magnetism to the nanoalloy energy, which makes these contributions included in our analysis, although in an indirect fashion. We did not observe any significant reconstruction in the calculated particles upon geometry optimization using DFT methods, such as the formation of new intermetallic bonds or cleavage of the existing bonds. If such reconstruction occurred, the obtained structures would be excluded from the fitting since the structure implied in the lattice Hamiltonian could not describe these nanoalloys.

Multiple linear regression was used to fit the energy descriptors ε_Y^X in equation (1) to minimize the differences between the energies of nanoalloys calculated using TOP Hamiltonian and DFT using the 5-fold cross-validation procedure implemented in the scikit-learn module.[66] The reported descriptors are the values obtained by averaging the descriptors obtained in the individual cross-validation fits. The root-mean-square error ($RMSE$) of the fitting was evaluated through the comparison of the relative energies of nanoalloys predicted from equation (1), E_{TOP}, to the same energies yielded by DFT calculations, E_{DFT}, by using the equation mentioned below:

$$RMSE = \sqrt{\frac{\Sigma(E_{DFT} - E_{TOP})^2}{N_{TRAIN} - N_{PAR}}},$$

Where E_{DFT} is the energy calculated through density functional theory calculations, E_{TOP} is the topological energy, N_{TRAIN} corresponds to the total number of structures considered in the training set and N_{PAR} corresponds to the total number of descriptors considered, which in this case equals 10. To determine 95% confidence intervals of energetic descriptors, we first determined their standard errors (SE) by calculating the square root of covariance of the data set containing E_{DFT} and structural descriptors. For a significance level of 0.05, we obtained a "t" value of 1.97 from

the t-table (for degrees of freedom equal to $N_{TRAIN} - N_{PAR}$). This "t" value was then multiplied with the standard error of individual descriptors to determine their 95% confidence intervals.

2.3 Monte Carlo calculations using the TOP method. The TOP lattice Hamiltonian described in equation (1) can be used to conduct highly efficient Monte Carlo (MC) simulations using the Metropolis algorithm implemented in a Python code publicly available on GitHub.[72] In the first approach, the temperature in MC simulations can be chosen sufficiently low to identify the lowest energy chemical ordering in the considered nanoalloy, which is in line with the global optimization approach employed extensively in the literature (Figure S2).[73,74] In the second approach, the temperature in simulations can be chosen equal to the temperature during synthesis or application of the considered material to generate nanoalloy models that realistically take into account the thermal disorder in the chemical ordering under given conditions.

In this study, we performed Metropolis Monte Carlo simulations employing canonical ensemble framework and using the TOP method for trimetallic truncated octahedral nanoparticles with fcc structure comprising 79 and 338 atoms with the size of 1.3 and 2.8 nm, respectively. For a nanoparticle containing 79 atoms, 1 million MC steps at a temperature of 40 K was enough to identify the lowest energy homotop, taking into account that each structure remained in its lowest energy state for over 50% of the simulation time at this temperature. The structures of 79-atom nanoparticles obtained from these MC simulations were recalculated with DFT to confirm their structural stability and low energy compared to other calculated structures for the respective alloy particle size and composition.

Previous studies on bimetallic nanoparticles showed that the fitting parameters are more sensitive to the composition of alloy nanoparticles rather than their size or shape.[37] These findings encouraged us to employ the descriptors fitted to DFT simulations of smaller nanoparticles to

much bigger species. For the 338-atom nanoparticles, the lowest-energy structures were obtained from MC simulations at 30 K with 50 million steps. To facilitate the convergence of such calculations, the energetic descriptors whose absolute values were below half of the thermal energy at room temperature (~13 meV) were set to zero.

In turn, to obtain realistic models of trimetallic nanoalloys at given temperatures, we conducted MC simulations for 10 million steps for 79-atom particles and 50 million steps for 338-atom nanoparticles. From these simulations, we selected representative structures that reflected the average structural properties of the ensemble as closely as possible.

2.4. Calculations of mixing energies. DFT mixing energy of a trimetallic nanoparticle can be calculated using the equation:

$$E_{mix}(A_xB_yC_z) = \frac{NE_{DFT}(A_xB_yC_z) - xE_{DFT}(A_N) - yE_{DFT}(B_N) - zE_{DFT}(C_N)}{N^2},$$

Where $N = x + y + z$ and $E_{DFT}(A_xB_yC_z)$ is the DFT energy of the trimetallic alloy nanoparticle, whereas $E_{DFT}(A_N)$, $E_{DFT}(B_N)$ and $E_{DFT}(C_N)$ are the energies of monometallic fcc nanoparticles with N atoms calculated with DFT. Similarly, the free energy of mixing can be calculated using the TOP method with the formula below, taking into account enthalpy and entropy of thermal disorder in the alloy:

$$G_{mix}(A_xB_yC_z) = \frac{NG_{TOP}(A_xB_yC_z) - xE_{TOP}(A_N) - yE_{TOP}(B_N) - zE_{TOP}(C_N)}{N^2}.$$

Here $E_{TOP}(A_N)$, $E_{TOP}(B_N)$ and $E_{TOP}(C_N)$ are the energies of monometallic nanoparticles with N atoms calculated using the TOP Hamiltonian. Within the methodology used, these energies are not affected by the thermal disorder at any temperature since all sites are populated by the same metal.

In turn, $G_{TOP}(A_xB_yC_z)$ is the free energy of the alloy nanoparticle calculated in a brute-force fashion as

$$G(A_xB_yC_z) = -k_BT \ln Q,$$

$$Q = N_{states} * \sum_{steps} \frac{1}{N_{steps}} \exp\left(-\frac{E_S(A_xB_yC_Z)}{k_BT}\right),$$

$$N_{states} = \frac{N!}{x!\,y!\,z!}.$$

In these formulas, N_{states} is the total number of states available to the system, N_{steps} is the total number of Monte-Carlo steps in the simulation, $E_S(A_xB_yC_Z)$ is the TOP energy of the system at a particular Monte-Carlo step s, k_B is the Boltzmann constant, and T is the assumed temperature for the simulations.

2.5 Details of DFT calculations. Spin-polarized DFT calculations involving 79-atom cuboctahedral trimetallic nanoparticles were performed using the VASP 6.3.2[75] with the revPBE exchange-correlation functional.[76] A projector augmented wave approach[77] was used to model the interaction between valence and core electrons. A plane-wave basis set with a cut-off energy of 415 eV was used. The electronic convergence criterion in the Konh-Sham SCF procedure was equal to 1×10^{-5} eV. The Fermi-Dirac smearing scheme was applied with a smearing width of 0.05 eV. D3 dispersion corrections with the Becke-Johnson damping function were employed.[78,79] The linear mixing parameter was set to 0.02 to dampen charge density fluctuations. Only the gamma point was considered in the reciprocal space because of the non-periodicity of the model systems.

The default conjugate gradient algorithm implemented in VASP was used for the relaxation of ion positions with the convergence criterion of 0.03 eV/Å for the maximal force component.

A vacuum of 10 Å was maintained between adjacent nanoparticles. All the nanoparticle shapes were constructed using the atomic simulation environment.[80] To obtain the Special Quasirandom Structures (SQS), the ATAT code[81] was used on a bulk system of a 2×2×2 supercell consisting of 128 atoms. Finally, a 79-atom SQS nanoparticle was constructed by removing some atoms from the obtained bulk alloy structure.

3. RESULTS AND DISCUSSION

We applied the extended TOP method to computationally characterize the chemical ordering in ~1.3 nm large $Ni_{26}Pd_{27}Cu_{26}$, $Pd_{26}Pt_{27}Cu_{26}$, and $Co_{26}Rh_{27}Cu_{26}$ alloys nanoparticles, which display different types of chemical ordering. In particular, we focused on the lowest energy chemical ordering (i.e., global minimum structure within the fixed nanoparticle lattice) and representative chemical orderings under typical application temperatures. The energetic descriptors in the topological Hamiltonians for these 79-atom nanoparticles were fitted to the energies of the nanoparticles of the same size, shape, and composition calculated using DFT. The RMSE of the fitted Hamiltonians amounts to 8-14 meV/atom. Such a degree of precision is significantly below the thermal energy at room temperature, 25 meV/atom, and allows one to design realistic models of trimetallic nanoalloys for most applications. Nevertheless, much higher precision of the TOP method was reported previously for bimetallic nanoparticles,[37] due to significantly lower mismatches between atomic sizes and simpler mixing patterns. In line with our previous studies,[37] the obtained energy descriptors were also used to characterize chemical ordering in much larger alloy nanoparticles whose direct calculations using DFT are not currently feasible.

To facilitate the discussion of various factors governing the nanocrystallite structure and stability, we analyze their contributions to the nanoalloy energy using the following metric:

$$E_{\%}(\varepsilon_Y^X) = 100\% * \varepsilon_Y^X N_Y^X \Big/ \sum_{i,j} \left|\varepsilon_j^i N_j^i\right|.$$

Note that $E_{\%}$ is positive for the structural features destabilizing the nanoparticle (i.e., increasing its energy) and negative for features increasing its thermodynamic stability.

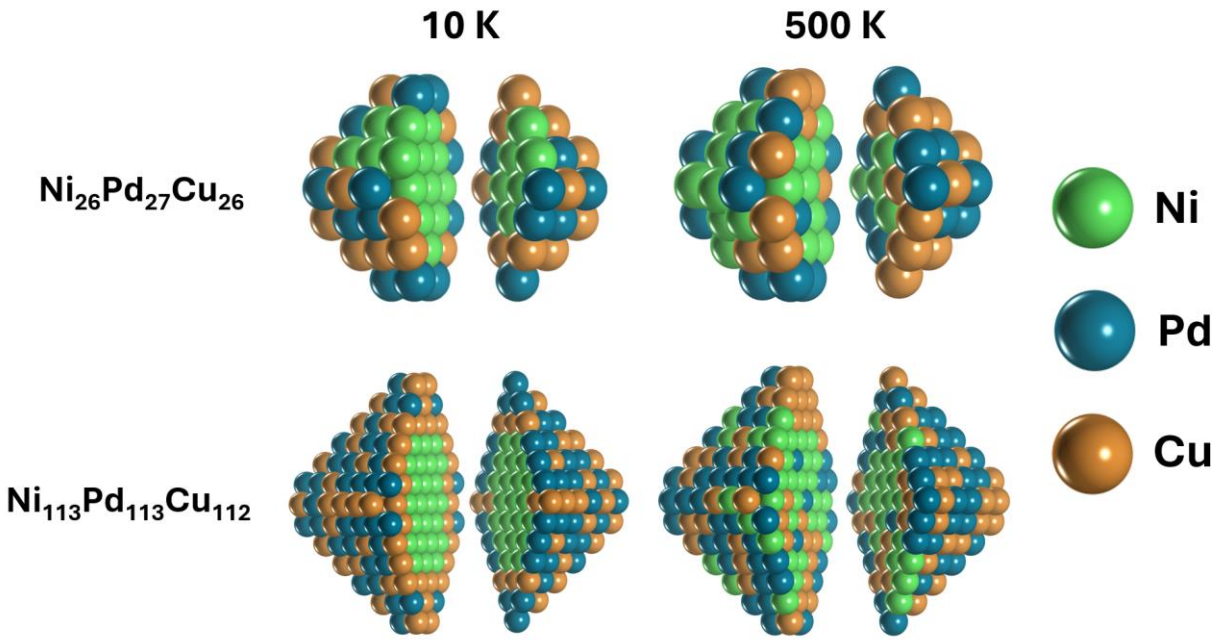

Figure 2. Representative structures of 1.3 nm and 2.8 nm large Ni-Pd-Cu nanoalloys at various temperatures.

3.1. Chemical ordering in Ni-Pd-Cu nanoalloys. According to our calculations, the low-temperature structure of Ni-Pd-Cu alloy nanocrystallites features Pd-rich Pd-Cu alloy on the surface and the core composed of either pure Ni or segregated Ni and Cu (Figure 2). In the lowest energy structure of $Ni_{26}Pd_{27}Cu_{26}$ nanoalloys, the nanoparticle core is composed of 19 Ni atoms, while the remaining 7 Ni atoms predominantly occupy terrace sites because there are no more core

sites available for them. On the surface, most of the edge sites are occupied by Cu (83%), whereas edge sites and terrace sites are occupied mostly by both Pd and Cu ($Ni_{0.04}Pd_{0.63}Cu_{0.33}$ composition for edges and $Ni_{0.21}Pd_{0.46}Cu_{0.33}$ for terraces). At 500 K, the core-shell structure is perturbed, with more Ni atoms occupying the terrace and edge sites and a few Pd and Cu atoms moving into the core region (Supplementary Table S1).

Table 1. Reference values for metal surface energies[82] (in J/m^2) and atomic radii[83] (in Å) of nanoalloy constituents.

Metal	Atomic radius	Surface energy[a]
Co	1.52	2.775
Ni	1.49	2.011
Cu	1.45	1.952
Rh	1.73	2.472
Pd	1.69	1.920
Pt	1.77	2.299

[a] The energy is given for the most stable surface, i.e. (111) for fcc metals and (0001) for hcp Co.

The Ni@PdCu core@shell structure of the nanoparticle is fully formed in larger $Ni_{113}Pd_{113}Cu_{112}$ at low temperatures. In this case, around 73% of the edge positions are occupied by Cu atoms, whereas the corner positions are populated by equal amounts of Cu and Pd atoms. In turn, 73% of terrace sites are occupied by Pd. At higher temperatures, the larger nanoparticles form a structure where around 23% of the total Ni atoms occupy the edge and terrace positions, whereas 9% of Pd atoms and 20% of Cu atoms move from the surface to the core (Table S2).

Table 2. Calculated energetic descriptors (in meV) for Ni-Pd-Cu, Pd-Pt-Cu, and Co-Rh-Cu nanoparticles. 95% confidence intervals are given for each descriptor value. The RMSE of the fitting is given in meV/atom.

$Ni_{26}Pd_{27}Cu_{26}$		$Pd_{26}Pt_{27}Cu_{26}$		$Co_{26}Rh_{27}Cu_{26}$	
$\varepsilon_{BOND}^{Ni-Cu}$	20 ± 7	$\varepsilon_{BOND}^{Pd-Cu}$	−27 ± 4	$\varepsilon_{BOND}^{Co-Cu}$	58 ± 6
$\varepsilon_{BOND}^{Pd-Cu}$	−29 ± 6	$\varepsilon_{BOND}^{Pt-Cu}$	−39 ± 4	$\varepsilon_{BOND}^{Rh-Cu}$	−3 ± 6
$\varepsilon_{BOND}^{Ni-Pd}$	−7 ± 6	$\varepsilon_{BOND}^{Pd-Pt}$	−5 ± 4	$\varepsilon_{BOND}^{Co-Rh}$	−23 ± 6
ε_{6}^{Ni}	231 ± 43	ε_{6}^{Pd}	−186 ± 38	ε_{6}^{Co}	427 ± 50
ε_{7}^{Ni}	154 ± 66	ε_{7}^{Pd}	−134 ± 57	ε_{7}^{Co}	449 ± 73
ε_{9}^{Ni}	167 ± 45	ε_{9}^{Pd}	−167 ± 37	ε_{9}^{Co}	254 ± 50
ε_{6}^{Pd}	−347 ± 71	ε_{6}^{Pt}	41 ± 40	ε_{6}^{Rh}	163 ± 68
ε_{7}^{Pd}	−304 ± 101	ε_{7}^{Pt}	−13 ± 57	ε_{7}^{Rh}	55 ± 97
ε_{9}^{Pd}	−299 ± 66	ε_{9}^{Pt}	−210 ± 35	ε_{9}^{Rh}	−66 ± 64
RMSE	13.6	RMSE	7.3	RMSE	12.2

The obtained structures of Ni-Pd-Cu nanoalloys can be rationalized from the known properties of constituting elements and the previous characterization of their bimetallic alloys. Indeed, the propensity of Ni to occupy core sites in Ni-Pd-Cu nanoparticles can be explained by the significantly higher surface energy of Ni compared to Pd and Cu (Table 1). As a result, the energetic descriptors for Ni segregation on low-coordinated sites in Ni-Pd-Cu particles are markedly positive, which leads to the small amount of Ni on the surface of low-energy Ni-Pd-Cu alloy nanoparticles. The preferential occupation of core sites by Ni was also noted in experimental and computational studies of bimetallic Pd-Ni[84,85] and Ni-Cu alloys.[86] Ni-Pd bond formation was calculated to be slightly exothermic with $\varepsilon_{BOND}^{Ni-Pd} - 7\ meV$. In turn, with the positive energy of the descriptor for Ni-Cu bond formation $\varepsilon_{BOND}^{Ni-Cu} = 20\ meV$ is in line with the previously noted

tendency to segregation in Ni-Cu alloys that depended on synthesis temperature (Table 2).[87] The formation of Pd-Cu bonds was exothermic, $\varepsilon_{BOND}^{Pd-Cu} = -29\ meV$, which aligns well with the propensity of Pd and Cu to form alloys in bulk and nanoparticle forms.[37,88,89]

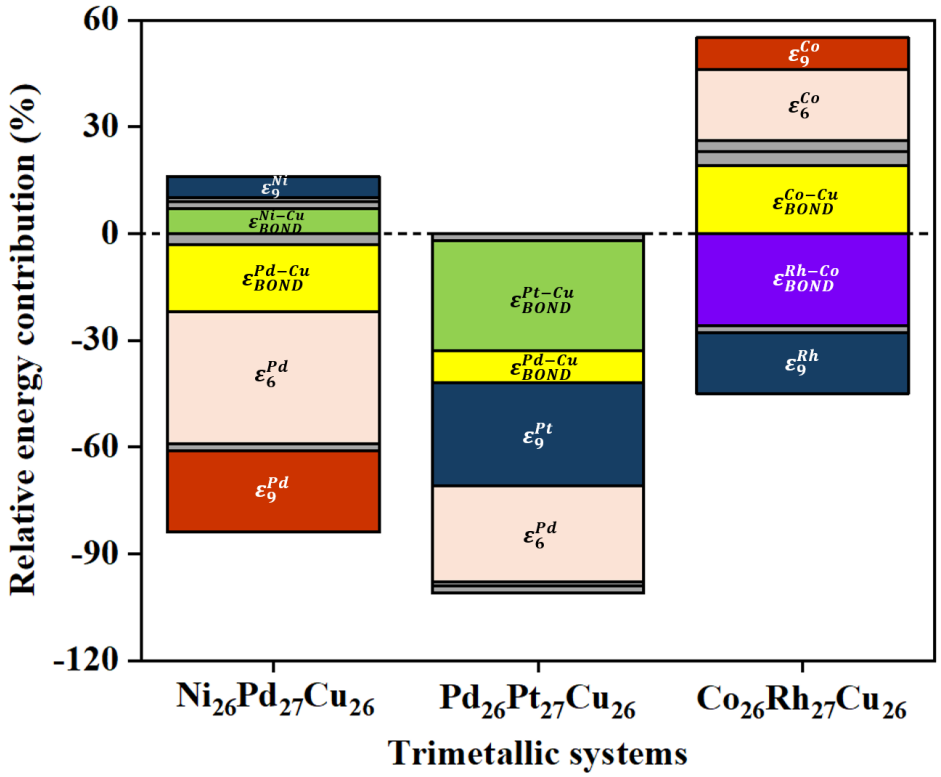

Figure 3. $E_{\%}$ metric for the relative energy contributions (%) to the topological energy of the lowest energy structures of $A_{26}B_{27}Cu_{26}$ according to DFT calculations. Only major contributions are labeled, whereas minor contributions are shown as gray boxes; see Table S1 for all the contributions.

The proposed rationalization of the structure of Ni-Pd-Cu nanoalloys through various factors can be quantified using the proposed $E_{\%}$ metric. The most important energetic contribution to the nanoparticle energy comes from the stabilization of Pd atoms on the NP surface, $E_{\%}(\varepsilon_6^{Pd}) = -37\%$ and $E_{\%}(\varepsilon_9^{Pd}) = -23\%$ (Figure 3 and Table S1). The surface is also populated by Cu

atoms in a way that maximizes the number of thermodynamically stable Pd-Cu bonds $E_{\%}\left(\varepsilon_{BOND}^{Pd-Cu}\right) = -19\%$ and minimizes thermodynamically unstable Cu-Ni bonds, $E_{\%}\left(\varepsilon_{BOND}^{Ni-Cu}\right) = 7\%$.

3.2. Chemical ordering in Pd-Pt-Cu nanoalloys. In turn, Pd-Pt-Cu nanoalloys develop a partially segregated structure with Cu-rich mixed Pd-Pt-Cu core and mostly Pd-Pt shell, which is in line with the "Pd-Pt dual site layer core-shell" structure of Pd-Pt-Cu alloys proposed experimentally.[67] The concentration of Cu in the core of $Pd_{26}Pt_{27}Cu_{26}$ amounts to 74% at low temperatures, whereas Pt occupies the rest of the core sites. As a result, the concentration of Cu atoms on the surface of $Pd_{26}Pt_{27}Cu_{26}$ is also notable (20%), although significantly less than concentrations of Pd and Pt (Figure 4). In particular, Pd atoms occupy almost all corner sites in the nanoparticle, whereas Pt occupies almost all terrace sites and Cu occupies most edge sites. As the temperature increases, the structure of $Pd_{26}Pt_{27}Cu_{26}$ turns into a well-mixed solid solution, with only 58% of the core occupied by Cu atoms, and the remaining core sites are occupied by Pd and Pt atoms. Cu atoms are also scattered on the corner (25% of corner sites), edge (58% of edge sites), and to a lesser extent on terrace sites. Similar to the low-temperature structure, the terrace sites of the high-temperature structure are also predominantly occupied by Pt atoms (80%). Around 63% of the corner sites and 42% of the edge sites are occupied by Pd atoms.

The bigger $Pd_{113}Pt_{113}Cu_{112}$ manifests a partially segregated structure more clearly, with the core containing a mixture of 61% Cu atoms, 37% Pt atoms, and just 2% Pd atoms. These Pd atoms are found in the first layer beneath the nanoparticle's surface. On the surface, Cu predominantly occupies the edge sites (31% of total edge sites) compared to terrace and corner sites. Pd atoms occupy all the corner sites of the bigger nanoparticle. In turn, the terraces of $Pd_{113}Pt_{113}Cu_{112}$ are occupied by Pd and Pt in roughly equal proportions. Some Pd atoms occupying the surface sites

migrate into the core at the increased temperature. This reduces the percentage of Pd atoms observed on the surface sites from 58% to 42% and increases the percentage of Pt atoms observed on the surface to 38%. Apart from that, a 70% increase is observed in the total number of Cu atoms on the surface sites.

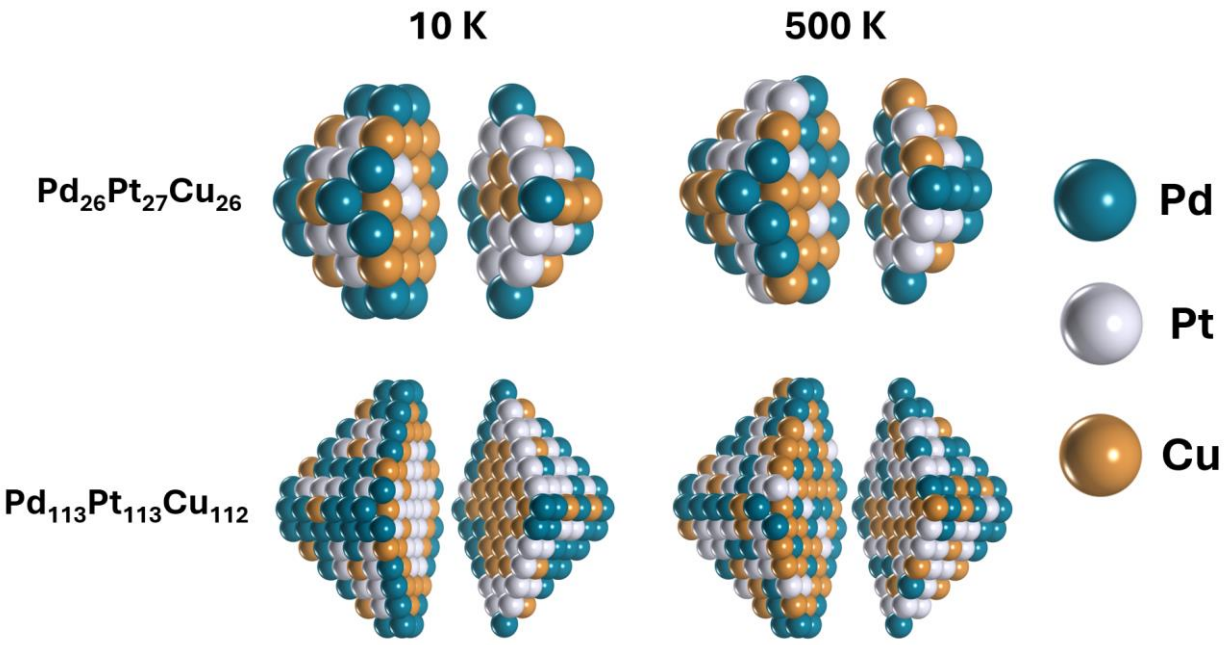

Figure 4. Representative structures of 1.3 nm and 2.8 nm large Pd-Pt-Cu nanoalloys at various temperatures.

The chemical ordering of elements within Pd-Pt-Cu alloy nanoparticles can be rationalized by the difference in the atomic sizes of the constituent elements, which outweighs rather moderate differences between their surface energies. Indeed, the core of these nanoalloys is composed mainly of smaller Cu atoms, whereas the surface is populated by larger Pd and Pt atoms. The segregation energies of Pd atoms on the NP surface are around -150 meV, whereas Pt segregation is thermodynamically favorable only on terrace sites with $\varepsilon_9^{Pt} = -210$ meV. The higher surface

concentration of Pd compared to Pt in our simulations aligns with previous computational studies of Pd-Pt bimetallic alloys.[42,90,91] In turn, the Cu-rich cores in the obtained structures are in line with core@shell structures developed by Cu@Pt alloys. [92] At the same time, bimetallic Pd-Cu alloys were shown through experiments[93] and simulations to form well-mixed structures,[37] which are also in line with the pronounced mixing between Pd and Cu in the Pd-Ni-Cu trimetallic nanoparticles considered above. However, in the obtained structures of Pd-Pt-Cu alloys, Pd atoms form more heteroatomic bonds with Pt atoms and a relatively insignificant amount of heteroatomic bonds with Cu. Thus, the presence of Pt in Pd-Pt-Cu alloy alters the usual mixing patterns between Pd and Cu observed in other alloys.

According to the $E_{\%}$ metric, the segregation of Pd and Pt to the nanoparticle surface contributes the most to the nanoparticle stability with $E_{\%}\left(\varepsilon_6^{Pd}\right) = -27\%$ and $E_{\%}(\varepsilon_9^{Pt}) = -29\%$, although the formation of Pd-Cu and Pt-Cu bonds are also important factors, with $E_{\%}\left(\varepsilon_{BOND}^{Pd-Cu}\right) = -9\%$ and $E_{\%}(\varepsilon_{BOND}^{Pt-Cu}) = -31\%$. The importance of the latter interactions results in the presence of some Pd and Pt atoms in the core of Pd-Pt-Cu nanoparticles and the emergence of some Cu atoms on the nanoalloy surface facilitated by the heteroatomic bond formation. The strength of Pd-Cu bonds was also noted in our previous studies of bimetallic particles.[37] In turn, the strength of Pd-Pt interactions was not significant enough to significantly affect the nanoparticle structure, which aligns with previous studies.[84]

3.3 Chemical ordering in Co-Rh-Cu nanoalloys. In principle, Co-Rh-Cu nanoalloys are calculated to adopt Co core @ Rh-Cu shell structure, i.e., the same type of structure as Pd-Ni-Cu (Figure 5). In the lowest energy structure of $Co_{26}Rh_{27}Cu_{26}$ nanoparticle, Co atoms occupy all core sites and ~15% of terrace and corner sites, where they are less stable. In turn, most (88%) of the terrace sites are occupied by Rh, with a few Rh atoms also present on edges and corners at a

concentration of 33% and 8%, respectively. Finally, Cu occupies 75% of the corner sites and 67% of the edge sites in the nanoparticle.

At higher temperatures, Co atoms move from the core of $Co_{26}Rh_{27}Cu_{26}$ NPs to the corners and edges, where their concentration increases to ~33%, although these sites were occupied entirely by Cu at low temperatures. Moreover, around 22% of the Rh atoms migrate to the core region, with the rest mainly remaining on terrace sites and, to a lesser extent, on edge sites.

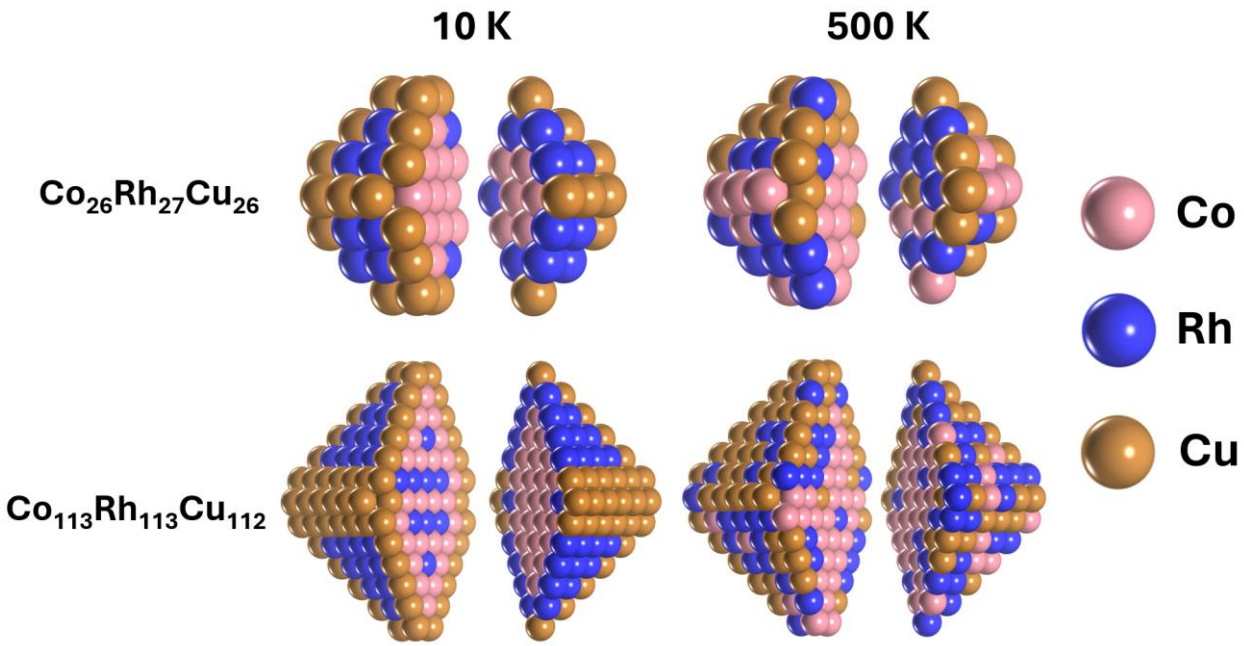

Figure 5. Representative structures of 1.3 nm and 2.8 nm large Co-Rh-Cu nanoalloys at various temperatures.

The qualitative differences between the structures of Co-Rh-Cu and Pd-Ni-Cu nanoalloys become more apparent for larger nanoparticles. Unlike $Ni_{113}Pd_{113}Cu_{112}$ particle, there is little mixing between elements in $Co_{113}Rh_{113}Cu_{112}$ particles due to the negligible exothermicity of Cu-Rh bonds and significant endothermicity of Cu-Co bonds with $\varepsilon_{BOND}^{Co-Cu} = 58$ meV. In the lowest energy structure of $Co_{113}Rh_{113}Cu_{114}$, the core is composed of Co-Rh alloy due to the exothermic

nature of Co-Rh bond formation with $\varepsilon_{BOND}^{Co-Rh} = -23$ meV. In turn, the edges and corners of these nanoparticles are composed of pure Cu, whereas the terraces predominantly expose Rh clusters (49% of the terrace sites). At higher temperatures, the thermal disorder in this structure leads to around 20% of the terrace sites being occupied by Co atoms. The percentage of Cu atoms found in the surface sites is also reduced by 20%, while the percentage of Rh atoms on the surface remains nearly the same. As expected, the thermal disorder also greatly reduces the clustering of the components in the alloy, which appears as a typical partially segregated core@shell structure at high temperatures.

The chemical ordering in Co-Rh-Cu can again be rationalized with the surface energies of the involved elements. For example, Cu has the lowest surface energy and occupies unsaturated corner and edge sites in the nanoparticles, whereas Co has the highest surface energy and occupies the core sites. Co segregation on the NP surface is significantly endothermic by >400 meV for edge and concern sites and by >250 meV for terrace sites, which is in line with Co@Cu core@shell structure of bimetallic CoCu NPs reported in some experiments.[94] Finally, Rh occupies the terrace sites with moderate coordination because its surface energy has an intermediate value between the surface energies of Co and Cu (Table 1). As a result, Rh exhibits insignificant surface segregation energies in our simulations, which aligns with small Rh segregation energies in bimetallic Rh-Cu alloys, where the segregation energies could even change sign depending on the alloy composition.[95] In addition, no conclusive evidence of surface Rh segregation can be found in previous experimental studies of Rh-Cu alloys, which report alloys with both Rh or Cu-rich surfaces.[96,97]

Analyzing the bond energy descriptors, we see that the formation of Co-Cu bonds is endothermic with an energy of 57.5 meV, which is in line with the facile segregation of Co and Cu into adjacent

monometallic NPs in catalysts for higher alcohol synthesis from CO.[98] In contrast, Co-Rh bond formation is markedly exothermic by −23 meV, which is in line with the tendency of Co and Rh to form well-mixed alloys.[98,99] The strong preference for Rh-Co bond formation, coupled with cobalt's propensity to occupy bulk sites, results in Rh atoms favoring terrace sites, where they are likely to interact with subsurface Co atoms (Figure 5). As a result of Rh-Co interactions, the segregation of Rh and Cu is induced in the nanoparticle despite the slight exothermicity of Rh-Cu bond formation (−2.6 meV).

According to our energy decomposition scheme, most of the stabilizing contributions in the case of $Co_{26}Rh_{27}Cu_{26}$ at low temperatures come from Rh-Co bonds, $E_{\%}\left(\varepsilon_{BOND}^{Rh-Co}\right) = -26\%$, and Rh segregation on terrace sites, $E_{\%}\left(\varepsilon_{9}^{Rh}\right) = -17\%$. The presence of Co atoms on the nanoparticle surface due to insufficient core sites to accommodate all Co atoms destabilizes the nanoparticle. Another destabilizing contribution comes from Cu-Co contacts, $E_{\%}(\varepsilon_{BOND}^{Co-Cu}) = 19\%$, which cannot be avoided in such small nanoparticles as $Co_{26}Rh_{27}Cu_{26}$ despite their endothermicity.[83]

3.4 The Reactivity of $Co_{26}Rh_{27}Cu_{26}$ Nanoparticles towards C Atoms. The reliable determination of chemical ordering in nanoalloys is of paramount importance for studies of their catalytic properties, which are governed to a large extent by the structure and composition of active sites developed on the nanoalloys' surface. To examine the effect of chemical ordering in nanoalloys on their reactivity, we examined the interactions of $Co_{26}Rh_{27}Cu_{26}$ nanoparticles with C atoms, which are key intermediates during coke formation.[100,101] Moreover, previous studies of linear scaling relations revealed that the binding energies of many reaction intermediates attaching to the surface via C atoms strongly correlate with the binding energies of isolated C atoms on the catalyst surface.[102] As a result, binding energies of C atoms to the catalyst surface are often used

as catalytic activity descriptors in the analysis of Sabatier volcano relations for the activity of various catalysts in a given reaction.[103]

Since chemical ordering in trimetallic nanoalloys is shown to depend on the simulation temperature significantly, we prepared three different models of $Co_{26}Rh_{27}Cu_{26}$ nanoparticles representing different application conditions (Figure 6). As the first model, we considered the nanoparticle structure with the lowest energy chemical ordering, which corresponds to the equilibrium structure of the nanoparticles at low temperatures (LT), e.g., ~10 K. In this structure, all core atoms were occupied by Co, and most of the terrace atoms were occupied by Rh, whereas Cu occupied most of the edge and corner sites. The second model was obtained as a representative structure from our Monte-Carlo simulations of $Co_{26}Rh_{27}Cu_{26}$ nanoparticles at a medium temperature (MT) of 573.15 K using the fitted lattice Hamiltonian. According to our DFT calculations, the MT structure of the $Co_{26}Rh_{27}Cu_{26}$ nanoparticle had 38 meV/atom (i.e., 2.97 eV per particle) higher energy than the low-temperature structure. In this structure of $Co_{26}Rh_{27}Cu_{26}$, a few Cu and Rh atoms penetrate into the nanoparticle bulk, and 4 Co atoms emerge on the low-coordinated sites on the surface, displacing Cu atoms previously occupying them onto the terrace sites. Finally, the structure of the alloy at high temperatures (HT) was obtained by using the ATAT code[81] to generate a special quasirandom structure (SQS), which maximizes the thermal disorder in the alloy. The high-temperature model was 127 meV/atom or 10.06 eV per particle higher in energy than our low-temperature structure, which should roughly correspond to the thermal energy at ~1500 K. The chemical ordering of alloy components in this structure shows no trends due to its quasirandom nature. Such structure could be obtained experimentally by rapid quenching of melted Co-Rh-Cu nanoparticles.

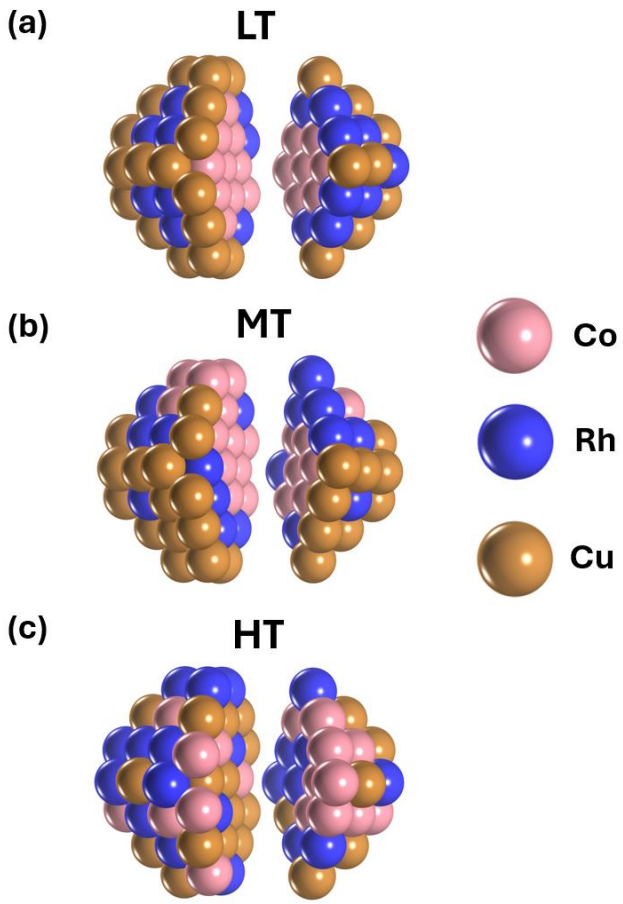

Figure 6. The considered low-temperature (LT), medium-temperature (MT), and special quasirandom high-temperature (HT) structures of the $Co_{26}Rh_{26}Cu_{27}$ nanoparticle. Table S3 contains the corresponding structural descriptors.

To investigate the differences between the reactivities of all these models, we modeled the adsorption of C atoms on each of the triangular hollow fcc and hcp sites on their surfaces. The obtained binding energy distributions show that sites containing Cu atoms tend to bind C atoms more weakly in all models, which could be expected because Cu is a coinage metal (Figure 7). The only exception to this trend is the presence of Cu in strongly binding sites in the high-temperature model. A closer look reveals that these sites have mixed CoRhCu composition, and the former two elements induce the strong binding energy of C on them. The analysis of these distributions also

reveals that Rh atoms are present in the composition of almost every hollow site on the surface in LT and MT models, whereas they are contained in a much lower number of hollow sites on the surface of the high-temperature model. Finally, Co-containing sites could be expected to bind C atoms very strongly due to the propensity of Co to form carbides.[14,104,105] However, the correlation between the C binding energy and the Co presence in the surface site composition is apparent only for low-temperature models. In contrast, MT and HT models show more complicated variations of C binding energies with the site composition.

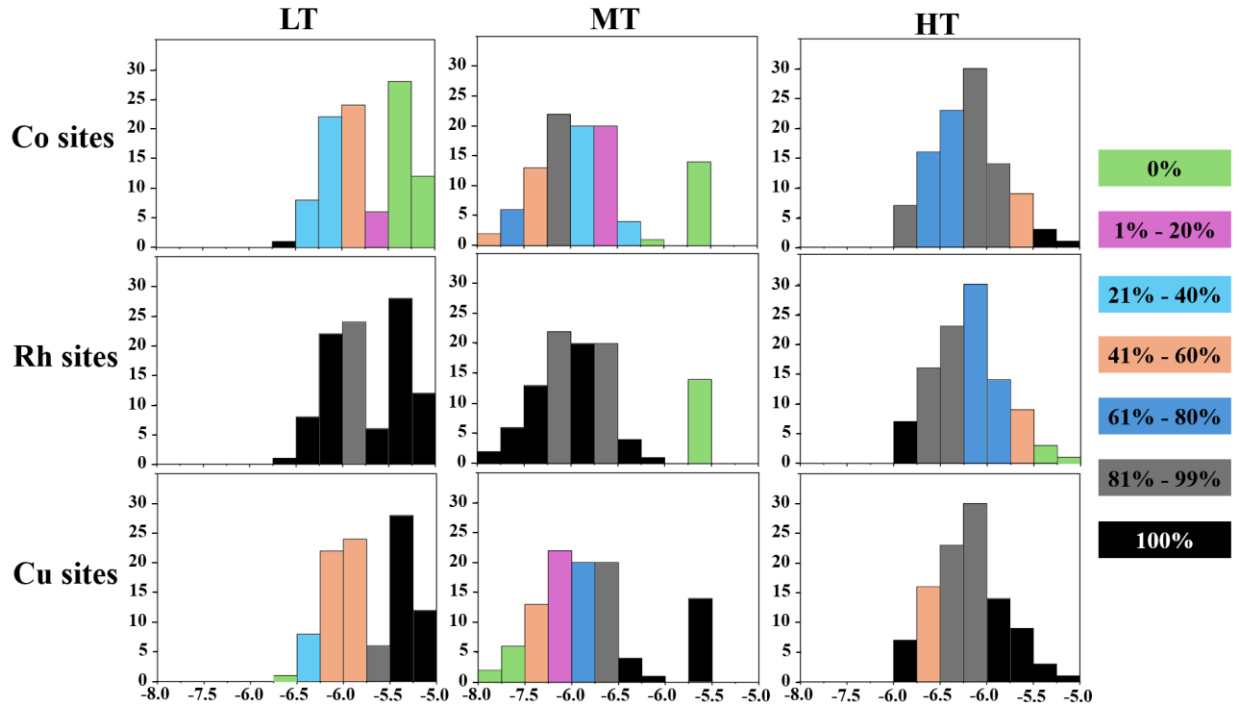

Figure 7. Histograms of carbon atom binding energies to the LT, MT, and HT structures of the $Co_{26}Rh_{27}Cu_{26}$ nanoparticle. The color coding of histogram bins indicates the proportion of hollow sites that include at least one Co, Rh, or Cu atom among the three atoms forming a hollow site on the (1 1 1) surface.

Due to the significant heterogeneity of the reactivities of various surface sites on the surface of $Co_{26}Rh_{26}Cu_{27}$ nanoalloys, it is more appropriate to analyze them statistically. On average, the binding strength of C was −5.74 ± 0.40 eV on the low-temperature model, −6.82 ± 0.57 eV on the medium-temperature model, and −6.17 ± 0.40 eV on quasirandom high-temperature model. Such temperature-induced changes in the reactivity of alloys towards C atoms would result in dramatic differences in the catalytic activity and stability of these nanoparticles in most applications. These findings highlight the necessity of selecting a nanoparticle model that accurately reflects the conditions of the considered application. Utilizing the proposed topological approach, we were able to generate reliable models of trimetallic nanoparticles with a realistic representation of thermal alloy disorder in only 90 minutes of computational time on a laptop.

3.5 Efficient Computation of Mixing Free Energies. To further demonstrate the exceptional computational efficiency of the proposed approach, we used the obtained topological Hamiltonians to calculate alloy mixing free energies through direct brute force evaluation of entropic contributions to the free energies of alloy nanoparticles through their partition functions. Namely, we evaluated the mixing free energies of trimetallic nanoparticles composed of 79 atoms for various alloy compositions at various temperatures (Figure 8). Whereas at the lowest considered temperature of 10 K, the free energy of alloy mixing is essentially determined by the energy of the lowest energy homotop, countless homotops contribute to the internal energy and entropy of mixing at higher temperatures.

Generally, each trimetallic nanoalloy is predicted to be miscible, i.e., to exhibit exothermic mixing energies for mixed compositions. Direct DFT calculations confirm the exothermic mixing in the obtained low-temperature structures of $Ni_{26}Pd_{27}Cu_{26}$, $Pd_{26}Pt_{27}Cu_{26}$, and $Co_{26}Rh_{27}Cu_{26}$ nanoparticles (Table S4). For a more profound analysis, we compare the obtained mixing energies

of trimetallic alloys to those of bimetallic alloys with structures optimized using the same TOP Hamiltonians as for trimetallic alloys (Figure S3).

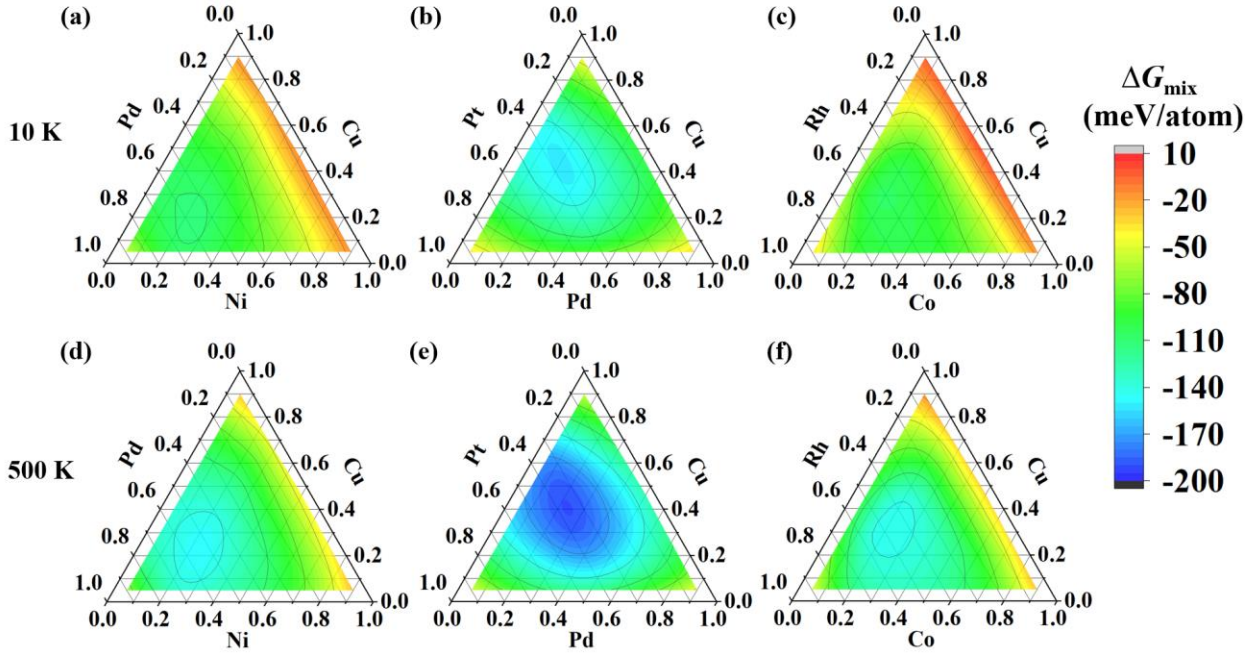

Figure 8. Mixing free energies of 79-atom Ni-Pd-Cu, Pd-Pt-Cu, and Co-Rh-Cu nanoalloys computed with Monte-Carlo simulations at 10 and 500 K. Mono- and bimetallic sectors in the diagrams were intentionally left blank.

In general, Ni-Pd-Cu nanoalloys become more stable at Pd-rich composition, achieving the most exothermic mixing energy at $Ni_{20}Pd_{47}Cu_{12}$ composition at 10 K and $Ni_{20}Pd_{43}Cu_{16}$ composition at 500 K, which can be explained by the weak binding between Ni and Cu. In this way, the presence of Pd in the composition of Ni-Pd-Cu alloys facilitates the mixing between Cu and Ni, whose calculated mixing energy in bimetallic Cu-Ni nanoalloy is close to zero or positive. Thus, our computational results align with the experimental evidence of facile phase separation in Ni-Cu alloys. [101]

In turn, all components in Pd-Pt-Cu alloys mix well, which is illustrated by the exothermic mixing energies of the respective bimetallic alloys. Pd-Pt-Cu nanoalloys generally are more stable in the Pd-poor region due to highly exothermic mixing between Pt and Cu. So, the most exothermic mixing is achieved with the $Pd_{12}Pt_{27}Cu_{40}$ composition of Pd-Pt-Cu at 10 K and with the $Pd_{20}Pt_{27}Cu_{32}$ composition at 500 K.

Finally, weak interactions between Co and Cu in Co-Rh-Cu alloys push the area of significant mixing energies towards Rh-rich compositions. In fact, bimetallic Co-Cu alloys are calculated to exhibit endothermic mixing energies, which suggest highly favorable separation between Co and Cu in line with experimental studies. [106,107] As a result, the highest magnitude of mixing energies is achieved at $Co_{12}Rh_{43}Cu_{24}$ composition at low temperatures and $Co_{16}Rh_{39}Cu_{24}$ composition at 500 K.

It should be noted that our analysis takes into account the contributions of the segregation of alloy components on terrace, edge, and corner sites of nanoparticles to their thermodynamic stability. Thus, these results are expected to be affected by the nanoparticle size, which governs the fraction of terrace, edge, and corner atoms in the nanoparticle structure.

4. SUMMARY

In conclusion, the developed method for designing realistic models of trimetallic alloy nanocrystallites allowed us to characterize the chemical ordering in Pd-Pt-Cu, Ni-Pd-Cu, and Co-Rh-Cu nanoparticles with fcc structures. This method was based on Monte-Carlo simulations using the proposed lattice Hamiltonian containing just 10 semi-empirical parameters with clear physical interpretation, whose values were fitted to the results of ~130 density functional calculations of nanoalloys via multiple linear regression. We proposed a training set composed of distinct archetypal chemical orderings that could be expected in nanoalloys based on chemical intuition to

make the fitting more robust. The high computational efficiency of the developed method allowed us to determine the chemical orderings with the lowest energy or with a realistic thermal disorder in alloy nanoparticles with 79 and 338 atoms. Moreover, we demonstrated the capabilities of the proposed method to calculate mixing free energies in the 79-atom alloy nanoparticles in a brute-force fashion through the direct evaluation of partition functions of nanoalloys. The Python code implementing this computational approach is openly accessible via GitHub.[72]

The obtained lowest-energy nanoalloy structures were in line with the previous experimental and computational studies of alloy nanoparticles composed of the respective metals and could be rationalized through physically meaningful fitting parameters in the employed Hamiltonians. For example, the high surface energy of Ni and strong Pd-Cu bonds stabilize the structure of Pd-Ni-Cu nanoparticles with Ni core and well-mixed Pd-Cu shell. In turn, the structure of Pd-Pt-Cu alloys is governed by the sizes of the involved atoms, which favor a higher concentration of smaller Cu atoms in the mixed Pd-Pt-Cu core and a larger concentration of well-mixed Pd and Pt in the nanoparticle shell. These findings align with the experimental characterization of the Pd-Pt-Cu nanoalloy structure in previous studies.[67] Finally, Co-Rh-Cu alloys also adopt a core-shell structure with Co in the core, whereas Rh and Cu form separated patches on the surface at low temperatures due to relatively weak Rh-Cu bonds.

However, the thermal disorder significantly affects the chemical ordering in these nanoparticles. In particular, the temperature is demonstrated to change the composition of adsorption sites on the nanoalloy surface and, hence, the reactivity of the alloy. For example, the average binding energy of C species on Co-Rh-Cu is calculated to change by up to 1.1 eV depending on the simulation temperature. Such changes would strongly affect the catalyst interaction with C-containing reaction intermediates and its propensity to form coke or carbide phases.

Thus, this study demonstrates the importance of thermal disorder for the reactivity of nanoalloys and proposes a highly efficient method (implemented in a freely available Python code) to generate models of trimetallic alloy nanoparticles with low energy or realistic thermal disorder. The models generated with this method will make simulations of nanoalloy catalysts more realistic and make their computational design more reliable.

ACKNOWLEDGEMENTS

This work is supported by Agency for Science, Technology and Research (A*STAR) through Low Carbon Energy Research Finding Initiative (LCERFI01–0033 | U2102d2006). Computational work was performed using resources of the National Supercomputing Centre, Singapore. The authors are grateful to Timothy D. Pook for technical support.

SUPPORTING INFORMATION

A PDF file containing supporting tables and mathematical formulae is provided.

CONFLICTS OF INTEREST

There are no conflicts of interest to declare.

KEYWORDS

Alloy nanoparticles, Nanoalloys, Global optimization, Trimetallic nanoparticles, Hydrogenation catalyst

REFERENCES

(1) Zhang, W.; Fu, Q.; Luo, Q.; Sheng, L.; Yang, J. Understanding Single-Atom Catalysis in View of Theory. *JACS Au* **2021**, *1* (12), 2130–2145. https://doi.org/10.1021/jacsau.1c00384.

(2) Singh, B.; Sharma, V.; Gaikwad, R. P.; Fornasiero, P.; Zbořil, R.; Gawande, M. B. Single-Atom Catalysts: A Sustainable Pathway for the Advanced Catalytic Applications. *Small* **2021**, *17* (16), 2006473. https://doi.org/10.1002/SMLL.202006473.
(3) He, T.; Santiago, A. R. P.; Kong, Y.; Ahsan, M. A.; Luque, R.; Du, A.; Pan, H. Atomically Dispersed Heteronuclear Dual-Atom Catalysts: A New Rising Star in Atomic Catalysis. *Small* **2022**, *18* (12), 2106091. https://doi.org/10.1002/SMLL.202106091.
(4) Hou, C. C.; Wang, H. F.; Li, C.; Xu, Q. From Metal–Organic Frameworks to Single/Dual-Atom and Cluster Metal Catalysts for Energy Applications. *Energy Environ Sci* **2020**, *13* (6), 1658–1693. https://doi.org/10.1039/C9EE04040D.
(5) Li, R.; Wang, D. Superiority of Dual-Atom Catalysts in Electrocatalysis: One Step Further Than Single-Atom Catalysts. *Adv Energy Mater* **2022**, *12* (9), 2103564. https://doi.org/10.1002/AENM.202103564.
(6) Pu, T.; Ding, J.; Zhang, F.; Wang, K.; Cao, N.; Hensen, E. J. M.; Xie, P. Dual Atom Catalysts for Energy and Environmental Applications. *Angewandte Chemie International Edition* **2023**, *62* (40), e202305964. https://doi.org/10.1002/ANIE.202305964.
(7) Hatta, A. H.; Jalil, A. A.; Hassan, N. S.; Hamid, M. Y. S.; Rahman, A. F. A.; Teh, L. P.; Prasetyoko, D. A Review on Recent Bimetallic Catalyst Development for Synthetic Natural Gas Production via CO Methanation. *Int J Hydrogen Energy* **2022**, *47* (72), 30981–31002. https://doi.org/10.1016/J.IJHYDENE.2021.10.213.
(8) Xie, Z.; Winter, L. R.; Chen, J. G. Bimetallic-Derived Catalysts and Their Application in Simultaneous Upgrading of CO_2 and Ethane. *Matter* **2021**, *4* (2), 408–440. https://doi.org/10.1016/J.MATT.2020.11.013.
(9) Crawley, J. W. M.; Gow, I. E.; Lawes, N.; Kowalec, I.; Kabalan, L.; Catlow, C. R. A.; Logsdail, A. J.; Taylor, S. H.; Dummer, N. F.; Hutchings, G. J. Heterogeneous Trimetallic Nanoparticles as Catalysts. *Chem Rev* **2022**, *122* (6), 6795–6849. https://doi.org/10.1021/acs.chemrev.1c00493.
(10) Chen, B. W. J.; Xu, L.; Mavrikakis, M. Computational Methods in Heterogeneous Catalysis. *Chem Rev* **2021**, *121* (2), 1007–1048. https://doi.org/10.1021/acs.chemrev.0c01060.
(11) Stratton, S. M.; Zhang, S.; Montemore, M. M. Addressing Complexity in Catalyst Design: From Volcanos and Scaling to More Sophisticated Design Strategies. *Surf Sci Rep* **2023**, *78* (3), 100597. https://doi.org/10.1016/J.SURFREP.2023.100597.
(12) Shambhawi, N.; Mohan, O.; Choksi, T. S.; Lapkin, A. A. The Design and Optimization of Heterogeneous Catalysts Using Computational Methods. *Catal Sci Technol* **2024**, *14* (3), 515–532. https://doi.org/10.1039/D3CY01160G.
(13) Bai, S.; Shao, Q.; Wang, P.; Dai, Q.; Wang, X.; Huang, X. Highly Active and Selective Hydrogenation of CO_2 to Ethanol by Ordered Pd-Cu Nanoparticles. *J Am Chem Soc* **2017**, *139* (20), 6827–6830. https://doi.org/10.1021/jacs.7b03101.
(14) Liu, S.; He, Y.; Fu, W.; Chen, J.; Ren, J.; Liao, L.; Sun, R.; Tang, Z.; Mebrahtu, C.; Zeng, F. Hetero-Site Cobalt Catalysts for Higher Alcohols Synthesis by CO_2 Hydrogenation: A Review. *Journal of CO2 Utilization* **2023**, *67*, 102322. https://doi.org/10.1016/J.JCOU.2022.102322.
(15) Khan, W. U.; Baharudin, L.; Choi, J.; Yip, A. C. K. Recent Progress in CO Hydrogenation over Bimetallic Catalysts for Higher Alcohol Synthesis. *ChemCatChem* **2021**, *13* (1), 111–120. https://doi.org/10.1002/CCTC.202001436.

(16) Zeng, F.; Mebrahtu, C.; Xi, X.; Liao, L.; Ren, J.; Xie, J.; Heeres, H. J.; Palkovits, R. Catalysts Design for Higher Alcohols Synthesis by CO_2 Hydrogenation: Trends and Future Perspectives. *Appl Catal B* **2021**, *291*, 120073. https://doi.org/10.1016/J.APCATB.2021.120073.
(17) Xu, D.; Wang, Y.; Ding, M.; Hong, X.; Liu, G.; Tsang, S. C. E. Advances in Higher Alcohol Synthesis from CO_2 Hydrogenation. *Chem* **2021**, *7* (4), 849–881. https://doi.org/10.1016/J.CHEMPR.2020.10.019.
(18) Mandal, S. C.; Das, A.; Roy, D.; Das, S.; Nair, A. S.; Pathak, B. Developments of the Heterogeneous and Homogeneous CO_2 Hydrogenation to Value-Added C_{2+}-Based Hydrocarbons and Oxygenated Products. *Coord Chem Rev* **2022**, *471*, 214737. https://doi.org/10.1016/J.CCR.2022.214737.
(19) Cao, S.; Sun, T.; Li, Q. Z.; Piao, L.; Chen, X. Solar-Driven H_2 Production from Formic Acid. *Trends Chem* **2023**, *5* (12), 947–960. https://doi.org/10.1016/j.trechm.2023.10.006.
(20) Younas, M.; Rezakazemi, M.; Arbab, M. S.; Shah, J.; Rehman, W. U. Green Hydrogen Storage and Delivery: Utilizing Highly Active Homogeneous and Heterogeneous Catalysts for Formic Acid Dehydrogenation. *Int J Hydrogen Energy* **2022**, *47* (22), 11694–11724. https://doi.org/10.1016/J.IJHYDENE.2022.01.184.
(21) Liu, M.; Xu, Y.; Meng, Y.; Wang, L.; Wang, H.; Huang, Y.; Onishi, N.; Wang, L.; Fan, Z.; Himeda, Y. Heterogeneous Catalysis for Carbon Dioxide Mediated Hydrogen Storage Technology Based on Formic Acid. *Adv Energy Mater* **2022**, *12* (31), 2200817. https://doi.org/10.1002/AENM.202200817.
(22) Mboyi, C. D.; Poinsot, D.; Roger, J.; Fajerwerg, K.; Kahn, M. L.; Hierso, J. C. The Hydrogen-Storage Challenge: Nanoparticles for Metal-Catalyzed Ammonia Borane Dehydrogenation. *Small* **2021**, *17* (44), 2102759. https://doi.org/10.1002/SMLL.202102759.
(23) Demirci, U. B. Mechanistic Insights into the Thermal Decomposition of Ammonia Borane, a Material Studied for Chemical Hydrogen Storage. *Inorg Chem Front* **2021**, *8* (7), 1900–1930. https://doi.org/10.1039/D0QI01366H.
(24) Yüksel Alpaydın, C.; Gülbay, S. K.; Ozgur Colpan, C. A Review on the Catalysts Used for Hydrogen Production from Ammonia Borane. *Int J Hydrogen Energy* **2020**, *45* (5), 3414–3434. https://doi.org/10.1016/J.IJHYDENE.2019.02.181.
(25) Dummer, N. F.; Willock, D. J.; He, Q.; Howard, M. J.; Lewis, R. J.; Qi, G.; Taylor, S. H.; Xu, J.; Bethell, D.; Kiely, C. J.; Hutchings, G. J. Methane Oxidation to Methanol. *Chem Rev* **2023**, *123* (9), 6359–6411. https://doi.org/10.1021/acs.chemrev.2c00439.
(26) Mendes, P. C. D.; Song, Y.; Ma, W.; Gani, T. Z. H.; Lim, K. H.; Kawi, S.; Kozlov, S. M. Opportunities in the Design of Metal@oxide Core-Shell Nanoparticles. *Adv Phys X* **2023**, *8* (1), 2175623. https://doi.org/10.1080/23746149.2023.2175623.
(27) Zhang, P.; Li, L.; Nordlund, D.; Chen, H.; Fan, L.; Zhang, B.; Sheng, X.; Daniel, Q.; Sun, L. Dendritic Core-Shell Nickel-Iron-Copper Metal/Metal Oxide Electrode for Efficient Electrocatalytic Water Oxidation. *Nature Communications 2018 9:1* **2018**, *9* (1), 1–10. https://doi.org/10.1038/s41467-017-02429-9.
(28) Ferrando, R.; Jellinek, J.; Johnston, R. L. Nanoalloys: From Theory to Applications of Alloy Clusters and Nanoparticles. *Chem Rev* **2008**, *108* (3), 845–910. https://doi.org/10.1021/cr040090g.

(29) Taran, S. Composition Effect on Melting Behaviors of Cu-Au-Pt Trimetallic Nanoalloys. *Comput Theor Chem* **2019**, *1166*, 112576. https://doi.org/10.1016/J.COMPTC.2019.112576.
(30) Garip, A. K.; Arslan, H.; Rapetti, D.; Ferrando, R. A DFT Study of Chemical Ordering and Oxygen Adsorption in AuPtPd Ternary Nanoalloys. *Mater Today Commun* **2020**, *25*, 101545. https://doi.org/10.1016/J.MTCOMM.2020.101545.
(31) Pacheco-Contreras, R.; Juárez-Sánchez, J. O.; Dessens-Félix, M.; Aguilera-Granja, F.; Fortunelli, A.; Posada-Amarillas, A. Empirical-Potential Global Minima and DFT Local Minima of Trimetallic $Ag_lAu_mPt_n$ (l + m + n = 13, 19, 33, 38) Clusters. *Comput Mater Sci* **2018**, *141*, 30–40. https://doi.org/10.1016/J.COMMATSCI.2017.09.022.
(32) Yoon, Y.; You, H. M.; Oh, J.; Lee, J. J.; Han, J. W.; Kim, K.; Kwon, H. Recent Advances in Atomic-Scale Simulations for Supported Metal Catalysts. *Molecular Catalysis* **2024**, *554*, 113862. https://doi.org/10.1016/J.MCAT.2024.113862.
(33) Li, H.; Jiao, Y.; Davey, K.; Qiao, S. Z. Data-Driven Machine Learning for Understanding Surface Structures of Heterogeneous Catalysts. *Angewandte Chemie International Edition* **2023**, *62* (9), e202216383. https://doi.org/10.1002/ANIE.202216383.
(34) Duan, X.; Han, Y.; Zhu, B.; Gao, Y. Modelling of Metal Nanoparticles' Structures and Dynamics under Reaction Conditions. *Materials Today Catalysis* **2023**, *3*, 100032. https://doi.org/10.1016/J.MTCATA.2023.100032.
(35) Kirchhoff, B.; Jung, C.; Gaissmaier, D.; Braunwarth, L.; Fantauzzi, D.; Jacob, T. In Silico Characterization of Nanoparticles. *Physical Chemistry Chemical Physics* **2023**, *25* (19), 13228–13243. https://doi.org/10.1039/D3CP01073B.
(36) Akbarzadeh, H.; Mehrjouei, E.; Abbaspour, M.; Shamkhali, A. N. Melting Behavior of Bimetallic and Trimetallic Nanoparticles: A Review of MD Simulation Studies. *Topics in Current Chemistry 2021 379:3* **2021**, *379* (3), 1–40. https://doi.org/10.1007/S41061-021-00332-Y.
(37) Kozlov, S. M.; Kovács, G.; Ferrando, R.; Neyman, K. M. How to Determine Accurate Chemical Ordering in Several Nanometer Large Bimetallic Crystallites from Electronic Structure Calculations. *Chem Sci* **2015**, *6* (7), 3868–3880. https://doi.org/10.1039/C4SC03321C.
(38) Huang, X.; Zhao, Z.; Cao, L.; Chen, Y.; Zhu, E.; Lin, Z.; Li, M.; Yan, A.; Zettl, A.; Wang, Y. M.; Duan, X.; Mueller, T.; Huang, Y. High-Performance Transition Metal-Doped Pt_3Ni Octahedra for Oxygen Reduction Reaction. *Science* **2015**, *348* (6240), 1230–1234. https://doi.org/10.1126/science.aaa8765.
(39) Jellinek, J.; Krissinel, E. B. NinAlm Alloy Clusters: Analysis of Structural Forms and Their Energy Ordering. *Chem Phys Lett* **1996**, *258* (1–2), 283–292. https://doi.org/10.1016/0009-2614(96)00636-7.
(40) Kadkhodaei, S.; Muñoz, J. A. Cluster Expansion of Alloy Theory: A Review of Historical Development and Modern Innovations. *JOM 2021 73:11* **2021**, *73* (11), 3326–3346. https://doi.org/10.1007/S11837-021-04840-6.
(41) Leong, Z.; Tan, T. L. Robust Cluster Expansion of Multicomponent Systems Using Structured Sparsity. *Phys Rev B* **2019**, *100* (13), 134108. https://doi.org/10.1103/PhysRevB.100.134108.
(42) Tan, T. L.; Wang, L. L.; Johnson, D. D.; Bai, K. A Comprehensive Search for Stable Pt-Pd Nanoalloy Configurations and Their Use as Tunable Catalysts. *Nano Lett* **2012**, *12* (9), 4875–4880. https://doi.org/10.1021/nl302405k.

(43) Wang, L. L.; Tan, T. L.; Johnson, D. D. Nanoalloy Electrocatalysis: Simulating Cyclic Voltammetry from Configurational Thermodynamics with Adsorbates. *Physical Chemistry Chemical Physics* **2015**, *17* (42), 28103–28111. https://doi.org/10.1039/C5CP00394F.

(44) Huang, X.; Zhao, Z.; Cao, L.; Chen, Y.; Zhu, E.; Lin, Z.; Li, M.; Yan, A.; Zettl, A.; Wang, Y. M.; Duan, X.; Mueller, T.; Huang, Y. High-Performance Transition Metal-Doped Pt_3Ni Octahedra for Oxygen Reduction Reaction. *Science* **2015**, *348* (6240), 1230–1234. https://doi.org/10.1126/science.aaa8765.

(45) Yan, Z.; Taylor, M. G.; Mascareno, A.; Mpourmpakis, G. Size-, Shape-, and Composition-Dependent Model for Metal Nanoparticle Stability Prediction. *Nano Lett* **2018**, *18* (4), 2696–2704. https://doi.org/10.1021/acs.nanolett.8b00670.

(46) Loevlie, D. J.; Ferreira, B.; Mpourmpakis, G. Demystifying the Chemical Ordering of Multimetallic Nanoparticles. *Acc Chem Res* **2023**, *56* (3), 248–257. https://doi.org/10.1021/acs.accounts.2c00646.

(47) Dean, J.; Cowan, M. J.; Estes, J.; Ramadan, M.; Mpourmpakis, G. Rapid Prediction of Bimetallic Mixing Behavior at the Nanoscale. *ACS Nano* **2020**, *14* (7), 8171–8180. https://doi.org/10.1021/acsnano.0c01586.

(48) Cheula, R.; Maestri, M.; Mpourmpakis, G. Modeling Morphology and Catalytic Activity of Nanoparticle Ensembles under Reaction Conditions. *ACS Catal* **2020**, *10* (11), 6149–6158. https://doi.org/10.1021/acscatal.0c01005.

(49) Dean, J.; Taylor, M. G.; Mpourmpakis, G. Unfolding Adsorption on Metal Nanoparticles: Connecting Stability with Catalysis. *Sci Adv* **2019**, *5* (9). https://doi.org/10.1126/sciadv.aax5101.

(50) Vega, L.; Aleksandrov, H. A.; Farris, R.; Bruix, A.; Viñes, F.; Neyman, K. M. Chemical Ordering in Pt–Au, Pt–Ag and Pt–Cu Nanoparticles from Density Functional Calculations Using a Topological Approach. *Mater Adv* **2021**, *2* (20), 6589–6602. https://doi.org/10.1039/D1MA00529D.

(51) Bau, J. A.; Kozlov, S. M.; Azofra, L. M.; Ould-Chikh, S.; Emwas, A. H.; Idriss, H.; Cavallo, L.; Takanabe, K. Role of Oxidized Mo Species on the Active Surface of Ni-Mo Electrocatalysts for Hydrogen Evolution under Alkaline Conditions. *ACS Catal* **2020**, *10* (21), 12858–12866. https://doi.org/10.1021/acscatal.0c02743.

(52) Kosari, M.; Anjum, U.; Xi, S.; Lim, A. M. H.; Seayad, A. M.; Raj, E. A. J.; Kozlov, S. M.; Borgna, A.; Zeng, H. C. Revamping SiO_2 Spheres by Core–Shell Porosity Endowment to Construct a Mazelike Nanoreactor for Enhanced Catalysis in CO_2 Hydrogenation to Methanol. *Adv Funct Mater* **2021**, *31* (47), 2102896. https://doi.org/10.1002/ADFM.202102896.

(53) Xie, X.; Briega-Martos, V.; Farris, R.; Dopita, M.; Vorokhta, M.; Skála, T.; Matolínová, I.; Neyman, K. M.; Cherevko, S.; Khalakhan, I. Optimal Pt-Au Alloying for Efficient and Stable Oxygen Reduction Reaction Catalysts. *ACS Appl Mater Interfaces* **2022**. https://doi.org/10.1021/acsami.2c18655.

(54) Wolfbeisser, A.; Kovács, G.; Kozlov, S. M.; Föttinger, K.; Bernardi, J.; Klötzer, B.; Neyman, K. M.; Rupprechter, G. Surface Composition Changes of CuNi-ZrO_2 during Methane Decomposition: An Operando NAP-XPS and Density Functional Study. *Catal Today* **2017**, *283*, 134–143. https://doi.org/10.1016/J.CATTOD.2016.04.022.

(55) Neitzel, A.; Kovács, G.; Lykhach, Y.; Kozlov, S. M.; Tsud, N.; Skála, T.; Vorokhta, M.; Matolín, V.; Neyman, K. M.; Libuda, J. Atomic Ordering and Sn Segregation in Pt–Sn

Nanoalloys Supported on CeO_2 Thin Films. *Top Catal* **2017**, *60* (6–7), 522–532. https://doi.org/10.1007/S11244-016-0709-5/METRICS.
(56) Sheng, Y.; Polynski, M. V.; Eswaran, M. K.; Zhang, B.; Lim, A. M. H.; Zhang, L.; Jiang, J.; Liu, W.; Kozlov, S. M. A Review of Mechanistic Insights into CO_2 Reduction to Higher Alcohols for Rational Catalyst Design. *Appl Catal B* **2024**, *343*, 123550. https://doi.org/10.1016/J.APCATB.2023.123550.
(57) Gao, P.; Zhang, L.; Li, S.; Zhou, Z.; Sun, Y. Novel Heterogeneous Catalysts for CO_2 Hydrogenation to Liquid Fuels. *ACS Cent Sci* **2020**, *6* (10), 1657–1670. https://doi.org/10.1021/acscentsci.0c00976.
(58) Zhao, Y. H.; Sun, K.; Ma, X.; Liu, J.; Sun, D.; Su, H. Y.; Li, W. X. Carbon Chain Growth by Formyl Insertion on Rhodium and Cobalt Catalysts in Syngas Conversion. *Angewandte Chemie International Edition* **2011**, *50* (23), 5335–5338. https://doi.org/10.1002/ANIE.201100735.
(59) Luk, H. T.; Mondelli, C.; Ferré, D. C.; Stewart, J. A.; Pérez-Ramírez, J. Status and Prospects in Higher Alcohols Synthesis from Syngas. *Chem Soc Rev* **2017**, *46* (5), 1358–1426. https://doi.org/10.1039/C6CS00324A.
(60) Liu, S.; Yang, C.; Zha, S.; Sharapa, D.; Studt, F.; Zhao, Z.-J.; Gong, J. Moderate Surface Segregation Promotes Selective Ethanol Production in CO_2 Hydrogenation Reaction over CoCu Catalysts. *Angewandte Chemie* **2022**, *134* (2), e202109027. https://doi.org/10.1002/ANGE.202109027.
(61) Xie, J. X.; Cao, J. P.; Zhao, X. Y.; Jiang, W.; Zhao, L.; Zhao, M.; Bai, H. C. Selective Cleavage of the Diphenyl Ether C-O Bond over a Ni Catalyst Supported on AC with Different Pore Structures and Hydrophilicities. *Energy and Fuels* **2021**, *35* (11), 9599–9608. https://doi.org/10.1021/acs.energyfuels.1c00809.
(62) Jiang, L.; Xu, G.; Fu, Y. Catalytic Cleavage of the C-O Bond in Lignin and Lignin-Derived Aryl Ethers over Ni/AlP_yO_xCatalysts. *ACS Catal* **2022**, *12* (15), 9473–9485. https://doi.org/10.1021/acscatal.2c01523.
(63) Xie, T.; Cao, J. P.; Zhu, C.; Zhao, X. Y.; Zhao, M.; Zhao, Y. P.; Wei, X. Y. Selective Cleavage of CO Bond in Benzyl Phenyl Ether over Pd/AC at Room Temperature. *Fuel Processing Technology* **2019**, *188*, 190–196. https://doi.org/10.1016/J.FUPROC.2019.02.022.
(64) Cao, A.; Schumann, J.; Wang, T.; Zhang, L.; Xiao, J.; Bothra, P.; Liu, Y.; Abild-Pedersen, F.; Nørskov, J. K. Mechanistic Insights into the Synthesis of Higher Alcohols from Syngas on CuCo Alloys. *ACS Catal* **2018**, *8* (11), 10148–10155. https://doi.org/10.1021/acscatal.8b01596.
(65) Zhao, Y. H.; Yang, M. M.; Sun, D.; Su, H. Y.; Sun, K.; Ma, X.; Bao, X.; Li, W. X. Rh-Decorated Cu Alloy Catalyst for Improved C_2 Oxygenate Formation from Syngas. *Journal of Physical Chemistry C* **2011**, *115* (37), 18247–18256. https://doi.org/10.1021/jp204961g.
(66) Xiong, B.; Liu, J.; Yang, Y.; Liu, W.; Chen, M.; Bai, H. Machine Learning-Assisted Screening of Cu-Based Trimetallic Catalysts for Electrochemical Conversion of CO_2 to CO. *Energy and Fuels* **2023**. https://doi.org/10.1021/acs.energyfuels.3c02359.
(67) Yang, X.; Yuan, Q.; Li, J.; Sheng, T.; Yao, K. X.; Wang, X. Subnanoscale Dual-Site Pd-Pt Layers Make PdPtCu Nanocrystals CO-Tolerant Bipolar Effective Electrocatalysts for Alcohol Fuel Cell Devices. *Nano Lett* **2023**, *23* (8), 3467–3475. https://doi.org/10.1021/acs.nanolett.3c00535.

(68) Coşkuner Filiz, B.; Kantürk Figen, A.; Pişkin, S. The Remarkable Role of Metal Promoters on the Catalytic Activity of Co-Cu Based Nanoparticles for Boosting Hydrogen Evolution: Ammonia Borane Hydrolysis. *Appl Catal B* **2018**, *238*, 365–380. https://doi.org/10.1016/J.APCATB.2018.07.031.
(69) You, D. J.; Kim, D. H.; De Lile, J. R.; Li, C.; Lee, S. G.; Kim, J. M.; Pak, C. Pd Core-Shell Alloy Catalysts for High-Temperature Polymer Electrolyte Membrane Fuel Cells: Effect of the Core Composition on the Activity towards Oxygen Reduction Reactions. *Appl Catal A Gen* **2018**, *562*, 250–257. https://doi.org/10.1016/J.APCATA.2018.06.018.
(70) Ryi, S. K.; Park, J. S.; Kim, S. H.; Kim, D. W.; Moon, J. W. Long-Term Hydrogen Permeation Tests of Pd–Cu–Ni/PNS with Temperature Cycles from Room Temperature to 773 K. *J Memb Sci* **2007**, *306* (1–2), 261–266. https://doi.org/10.1016/J.MEMSCI.2007.08.048.
(71) Nayebossadri, S.; Speight, J. D.; Book, D. Pd-Cu-M (M = Y, Ti, Zr, V, Nb, and Ni) Alloys for the Hydrogen Separation Membrane. *ACS Appl Mater Interfaces* **2017**, *9* (3), 2650–2661. https://doi.org/10.1021/acsami.6b12752.
(72) *Computational-Nanocatalysis-Group/Trimetallic-Monte-Carlo: This repository contains a simple python code for performing Monte-Carlo simulation of Trimetallic nanoparticles*. https://github.com/Computational-Nanocatalysis-Group/Trimetallic-Monte-Carlo (accessed 2024-04-30).
(73) Barcaro, G.; Sementa, L.; Fortunelli, A. A Grouping Approach to Homotop Global Optimization in Alloy Nanoparticles. *Physical Chemistry Chemical Physics* **2014**, *16* (44), 24256–24265. https://doi.org/10.1039/C4CP03745F.
(74) Rapetti, D.; Roncaglia, C.; Ferrando, R. Optimizing the Shape and Chemical Ordering of Nanoalloys with Specialized Walkers. *Adv Theory Simul* **2023**, *6* (9), 2300268. https://doi.org/10.1002/ADTS.202300268.
(75) Kresse, G.; Furthmüller, J. Efficient Iterative Schemes for *Ab Initio* Total-Energy Calculations Using a Plane-Wave Basis Set. *Phys Rev B* **1996**, *54* (16), 11169–11186. https://doi.org/10.1103/PhysRevB.54.11169.
(76) Zhang, Y.; Yang, W. Comment on "Generalized Gradient Approximation Made Simple." *Phys Rev Lett* **1998**, *80* (4), 890. https://doi.org/10.1103/PhysRevLett.80.890.
(77) Kresse, G.; Joubert, D. From Ultrasoft Pseudopotentials to the Projector Augmented-Wave Method. *Phys Rev B* **1999**, *59* (3), 1758–1775. https://doi.org/10.1103/PhysRevB.59.1758.
(78) Grimme, S.; Antony, J.; Ehrlich, S.; Krieg, H. A Consistent and Accurate *Ab Initio* Parametrization of Density Functional Dispersion Correction (DFT-D) for the 94 Elements H-Pu. *J Chem Phys* **2010**, *132* (15), 154104. https://doi.org/10.1063/1.3382344.
(79) Grimme, S.; Ehrlich, S.; Goerigk, L. Effect of the Damping Function in Dispersion Corrected Density Functional Theory. *J Comput Chem* **2011**, *32* (7), 1456–1465. https://doi.org/10.1002/jcc.21759.
(80) Hjorth Larsen, A.; JØrgen Mortensen, J.; Blomqvist, J.; Castelli, I. E.; Christensen, R.; Dułak, M.; Friis, J.; Groves, M. N.; Hammer, B.; Hargus, C.; Hermes, E. D.; Jennings, P. C.; Bjerre Jensen, P.; Kermode, J.; Kitchin, J. R.; Leonhard Kolsbjerg, E.; Kubal, J.; Kaasbjerg, K.; Lysgaard, S.; Bergmann Maronsson, J.; Maxson, T.; Olsen, T.; Pastewka, L.; Peterson, A.; Rostgaard, C.; SchiØtz, J.; Schütt, O.; Strange, M.; Thygesen, K. S.; Vegge, T.; Vilhelmsen, L.; Walter, M.; Zeng, Z.; Jacobsen, K. W. The Atomic Simulation

Environment—a Python Library for Working with Atoms. *Journal of Physics: Condensed Matter* **2017**, *29* (27), 273002. https://doi.org/10.1088/1361-648X/AA680E.
(81) Van de Walle, A.; Asta, M.; Ceder, G. The Alloy Theoretic Automated Toolkit: A User Guide. *Calphad* **2002**, *26* (4), 539–553. https://doi.org/10.1016/S0364-5916(02)80006-2.
(82) Vitos, L.; Ruban, A. V.; Skriver, H. L.; Kollár, J. The Surface Energy of Metals. *Surf Sci* **1998**, *411* (1–2), 186–202. https://doi.org/10.1016/S0039-6028(98)00363-X.
(83) Clementi, E.; Raimondi, D. L.; Reinhardt, W. P. Atomic Screening Constants from SCF Functions. II. Atoms with 37 to 86 Electrons. *J Chem Phys* **1967**, *47* (4), 1300–1307. https://doi.org/10.1063/1.1712084.
(84) Datta, S.; Ghosh, A.; Saha-Dasgupta, T. First Principles Insights into the Relative Stability, Electronic and Catalytic Properties of Core–Shell, Janus and Mixed Structural Patterns for Bimetallic Pd–X Nano-Alloys (X = Co, Ni, Cu, Rh, Ag, Ir, Pt, Au). *Physical Chemistry Chemical Physics* **2023**, *25* (6), 4667–4679. https://doi.org/10.1039/D2CP04342D.
(85) Xiang, J.; Li, P.; Chong, H.; Feng, L.; Fu, F.; Wang, Z.; Zhang, S.; Zhu, M. Bimetallic Pd-Ni Core-Shell Nanoparticles as Effective Catalysts for the Suzuki Reaction. *Nano Res* **2014**, *7* (9), 1337–1343. https://doi.org/10.1007/S12274-014-0498-8.
(86) Wolfbeisser, A.; Kovács, G.; Kozlov, S. M.; Föttinger, K.; Bernardi, J.; Klötzer, B.; Neyman, K. M.; Rupprechter, G. Surface Composition Changes of CuNi-ZrO_2 during Methane Decomposition: An Operando NAP-XPS and Density Functional Study. *Catal Today* **2017**, *283*, 134–143. https://doi.org/10.1016/J.CATTOD.2016.04.022.
(87) Guisbiers, G.; Khanal, S.; Ruiz-Zepeda, F.; Roque De La Puente, J.; José-Yacaman, M. Cu–Ni Nano-Alloy: Mixed, Core–Shell or Janus Nano-Particle? *Nanoscale* **2014**, *6* (24), 14630–14635. https://doi.org/10.1039/C4NR05739B.
(88) Chau, Y. T. R.; Nguyen, M. T.; Zhu, M.; Romier, A.; Tokunaga, T.; Yonezawa, T. Synthesis of Composition-Tunable Pd–Cu Alloy Nanoparticles by Double Target Sputtering. *New Journal of Chemistry* **2020**, *44* (12), 4704–4712. https://doi.org/10.1039/D0NJ00288G.
(89) Volkov, A. Y.; Novikova, O. S.; Antonov, B. D. The Kinetics of Ordering in an Equiatomic CuPd Alloy: A Resistometric Study. *J Alloys Compd* **2013**, *581*, 625–631. https://doi.org/10.1016/J.JALLCOM.2013.07.132.
(90) Rodríguez-Proenza, C. A.; Palomares-Báez, J. P.; Chávez-Rojo, M. A.; García-Ruiz, A. F.; Azanza-Ricardo, C. L.; Santoveña-Uribe, A.; Luna-Bárcenas, G.; Rodríguez-López, J. L.; Esparza, R. Atomic Surface Segregation and Structural Characterization of PdPt Bimetallic Nanoparticles. *Materials* **2018**, *11* (10), 1882. https://doi.org/10.3390/MA11101882.
(91) Ishimoto, T.; Koyama, M. Electronic Structure and Phase Stability of PdPt Nanoparticles. *Journal of Physical Chemistry Letters* **2016**, *7* (5), 736–740. https://doi.org/10.1021/acs.jpclett.5b02753.
(92) Vega, L.; Garcia-Cardona, J.; Viñes, F.; Cabot, P. L.; Neyman, K. M. Nanostructuring Determines Poisoning: Tailoring CO Adsorption on PtCu Bimetallic Nanoparticles. *Mater Adv* **2022**, *3* (10), 4159–4169. https://doi.org/10.1039/D2MA00196A.
(93) Gu, Z.; Xiong, Z.; Ren, F.; Li, S.; Xu, H.; Yan, B.; Du, Y. Flower-like PdCu Catalyst with High Electrocatalytic Properties for Ethylene Glycol Oxidation. *J Taiwan Inst Chem Eng* **2018**, *83*, 32–39. https://doi.org/10.1016/J.JTICE.2017.12.010.

(94) Golub, K. W.; Sulmonetti, T. P.; Darunte, L. A.; Shealy, M. S.; Jones, C. W. Metal-Organic-Framework-Derived Co/Cu-Carbon Nanoparticle Catalysts for Furfural Hydrogenation. *ACS Appl Nano Mater* **2019**, *2* (9), 6040–6056. https://doi.org/10.1021/acsanm.9b01555.
(95) Ellison, K. A.; Underhill, P. R.; Smeltzer, W. W. High Temperature Surface Segregation on Cobalt-Rhodium Alloys Using Auger Electron Spectroscopy. *Surf Sci* **1987**, *182* (1–2), 69–84. https://doi.org/10.1016/0039-6028(87)90089-6.
(96) Foucher, A. C.; Yang, S.; Rosen, D. J.; Lee, J. D.; Huang, R.; Jiang, Z.; Barrera, F. G.; Chen, K.; Hollyer, G. G.; Friend, C. M.; Gorte, R. J.; Murray, C. B.; Stach, E. A. Synthesis and Characterization of Core-Shell Cu-Ru, Cu-Rh, and Cu-Ir Nanoparticles. *J Am Chem Soc* **2022**, *144* (17), 7919–7928. https://doi.org/10.1021/jacs.2c02538.
(97) Meitzner, G.; Via, G. H.; Lytle, F. W.; Sinfelt, J. H. Structure of Bimetallic Clusters. Extended X-ray Absorption Fine Structure (EXAFS) Studies of Rh–Cu Clusters. *J Chem Phys* **1983**, *78* (2), 882–889. https://doi.org/10.1063/1.444789.
(98) Göbel, C.; Schmidt, S.; Froese, C.; Fu, Q.; Chen, Y. T.; Pan, Q.; Muhler, M. Structural Evolution of Bimetallic Co-Cu Catalysts in CO Hydrogenation to Higher Alcohols at High Pressure. *J Catal* **2020**, *383*, 33–41. https://doi.org/10.1016/J.JCAT.2020.01.004.
(99) Fromen, M. C.; Lecante, P.; Casanove, M. J.; Guiliemaud, G. B.; Zitoun, D.; Amiens, C.; Chaudret, B.; Respaud, M.; Benfield, R. E. Structural Study of Bimetallic CoxRh1-x Nanoparticles: Size and Composition Effects. *Phys Rev B* **2004**, *69* (23), 235416. https://doi.org/10.1103/PhysRevB.69.235416.
(100) Kozlov, S. M.; Yudanov, I. V.; Aleksandrov, H. A.; Rösch, N. Theoretical Study of Carbon Species on Pd(111): Competition between Migration of C Atoms to the Subsurface Interlayer and Formation of Cnclusters on the Surface. *Physical Chemistry Chemical Physics* **2009**, *11* (46), 10955–10963. https://doi.org/10.1039/B916855A.
(101) Bu, K.; Kang, Y.; Li, Y.; Zhang, Y.; Tang, Y.; Huang, Z.; Shen, W.; Xu, H. CO2-Assisted Propane Dehydrogenation to Aromatics over Copper Modified Ga-MFI Catalysts. *Appl Catal B* **2024**, *343*, 123528. https://doi.org/10.1016/J.APCATB.2023.123528.
(102) Abild-Pedersen, F.; Greeley, J.; Studt, F.; Rossmeisl, J.; Munter, T. R.; Moses, P. G.; Skúlason, E.; Bligaard, T.; Nørskov, J. K. Scaling Properties of Adsorption Energies for Hydrogen-Containing Molecules on Transition-Metal Surfaces. *Phys Rev Lett* **2007**, *99* (1), 016105. https://doi.org/10.1103/PhysRevLett.99.016105.
(103) Jones, G.; Jakobsen, J. G.; Shim, S. S.; Kleis, J.; Andersson, M. P.; Rossmeisl, J.; Abild-Pedersen, F.; Bligaard, T.; Helveg, S.; Hinnemann, B.; Rostrup-Nielsen, J. R.; Chorkendorff, I.; Sehested, J.; Nørskov, J. K. First Principles Calculations and Experimental Insight into Methane Steam Reforming over Transition Metal Catalysts. *J Catal* **2008**, *259* (1), 147–160. https://doi.org/10.1016/J.JCAT.2008.08.003.
(104) ten Have, I. C.; Weckhuysen, B. M. The Active Phase in Cobalt-Based Fischer-Tropsch Synthesis. *Chem Catalysis* **2021**, *1* (2), 339–363. https://doi.org/10.1016/J.CHECAT.2021.05.011.
(105) Fei Tan, K.; Xu, J.; Chang, J.; Borgna, A.; Saeys, M. Carbon Deposition on Co Catalysts during Fischer–Tropsch Synthesis: A Computational and Experimental Study. *J Catal* **2010**, *274* (2), 121–129. https://doi.org/10.1016/J.JCAT.2010.06.008.
(106) Miranda, M.; Estévez-Rams, E.; Martínez, G.; Baibich, N. Phase Separation in $Cu_{90}Co_{10}$ High-Magnetoresistance Materials. *Phys Rev B* **2003**, *68* (1), 014434. https://doi.org/10.1103/PhysRevB.68.014434.

(107) Farzam, F.; Bellón, B.; Chatain, D.; Jiménez, J. A.; Breitbach, B.; Ghidelli, M.; Jazmin Duarte, M.; Dehm, G. Decomposition and Dewetting of Super-Saturated Cu-15 at. % Co Solid Solution Film. *Mater Des* **2024**, *241*, 112892. https://doi.org/10.1016/J.MATDES.2024.112892.